

Bubble dynamics in a cavitating venturi

Premchand V Chandra^{1,2*}, Anuja Vijayan^{2,*}, and Pradeep Kumar^{2,*}

¹*Indian Institute of Science Bangalore, India*

²*Indian Institute of Space Science and Technology, Trivandrum, India*
^{1,2,3} (***equal contributions**; email: premchandv@iisc.ac.in)

December 30, 2024

Abstract

Cryogenic fluids are widely used as fuel for launch vehicles and many other industrial applications. The physics of cryogenic flows is highly complex due to their sensitivity to phase changes. Because of their low boiling points, cryogenic liquids undergo phase transition from liquid to bubbly liquid to vapour. This leads to cavitating flows that fall under the two-phase flow regime. This study models bubbly flows of cryogenic fluids, specifically liquid nitrogen, in a converging-diverging venturi device known as a cavitating venturi, a passive flow control and measurement device. Existing numerical studies in the literature are mostly limited to isothermal bubbly flows, such as water, where energy equations are often neglected due to minimal heat transfer at the interface. In contrast, cryogenic fluids are highly sensitive to phase changes under ambient conditions and interface heat transfer plays a significant role owing to their low latent heat of vaporization. To develop an appropriate model for cryogenic bubbly flows, we incorporate the effects of convective heat transfer from the quiescent liquid to the traversing bubble and heat transfer at the bubble-fluid interface. The numerical modelling is carried out using an in-house finite-difference code, and the results highlight the critical influence of heat transport equations on bubble dynamics. A commercial CFD package is used for two-dimensional simulations to complement the in-house simulations to predict cavitation length, a key characterizing parameter. In addition, limited flow visualization experiments are performed using a high-speed camera to analyze the length of the cavitation zone. This combined numerical and experimental approach provides valuable insight into the dynamics of cryogenic bubbly flows in cavitating venturi systems.

1 Introduction

A cavitating venturi is a simple, passive flow control and metering device that maintains a constant mass flow rate of fluid, even when downstream pressure conditions fluctuate. The venturi consists of three key sections: a converging section, a throat, and a diverging section. The throat, having the minimum cross-sectional area, causes the fluid pressure to drop to its lowest point as the flow passes through it. When the fluid pressure near the throat reaches its vapour pressure, vapour cavities or bubbles begin to form, initiating cavitation [1]. In a cavitating venturi, the flow exhibits a mix of behaviours, including bubble formation, growth, collapse, and dynamic interactions such as fission, fusion, re-entrant jet formation, and turbulent mixing of vapour bubbles as the flow moves from the throat into the diverging section. These characteristics are typical of cavitating two-phase flows. Lord Rayleigh's [2] work was one of the earlier works on cavitation dynamics. Plesset et al. [3] put forth a modified bubble dynamics equation for the present numerical work. Many theoretical, numerical, and experimental verification literature exists on cavitating flows and in particular the cavitating flows in converging diverging nozzles or cavitating venturi [4]-[10]. Cavitating flow is a well-known two-phase phenomenon commonly encountered in mechanical systems such as turbo pumps (near the inducer) and marine propellers. In pumps operating at high rotational speeds, the pressure near the inducer can drop to levels that induce vapour formation, resulting in cavitation patterns such as attached cavitation and travelling bubble cavitation. These cavitation patterns are often observed in

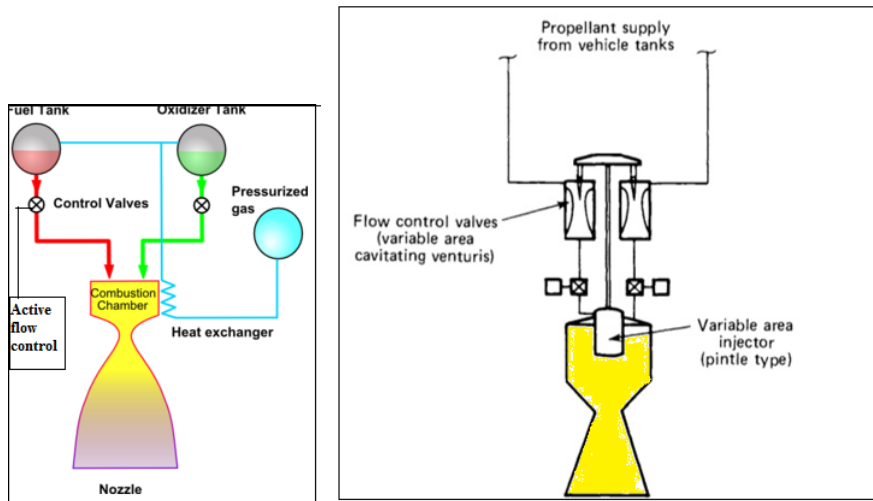


Figure 1: Rocket Propulsion systems with (a). Active Flow device, and (b). Passive flow device

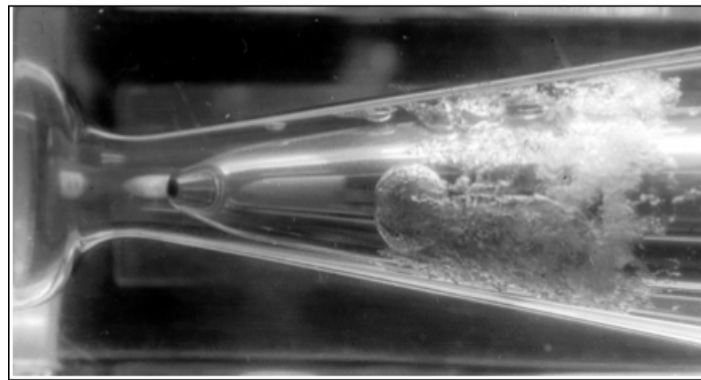


Figure 2: Developed cavitation in a Venturi device [1]

other turbomachines and can cause significant damage, including erosion of impeller vane surfaces, which ultimately shortens the service life. Despite its detrimental effects on many mechanical systems, cavitation can benefit passive flow control devices such as cavitating venturi. The figure below (Figure 2) illustrates the development of cavitation in a typical cavitating venturi.

As a passive flow measurement device, a cavitating venturi eliminates the need for complex control valves and actuating systems. Instead, it leverages the choked flow principle to maintain a constant flow rate, regardless of downstream pressure variations. Figure 2 illustrates developed cavitation in a venturi.

Rocket propulsion systems rely on flow control to deliver liquid propellants to combustion chambers. While active systems involve control valves and actuators, their reliability is compromised by mechanical complexity. In contrast, a cavitating venturi serves as a reliable passive alternative, using cavitation-induced flow restriction to stabilize the flow rate.

In a cavitating venturi:

- (a). For compressible flows, choked flow occurs as fluid accelerates to sonic velocity at the throat, preventing upstream pressure propagation.
- (b). For incompressible flows, evaporation occurs before sonic velocity is reached, forming vapor bubbles near the throat. These bubbles restrict the flow, ensuring a stable flow rate.
- (c). Downstream, pressure recovery collapses the vapor bubbles, restoring single-phase flow.

This unique property makes cavitating venturi ideal for liquid and cryogenic rocket engines, where flow remains steady despite fluctuations in combustion chamber pressure. Cryogenic cavitating flows, due to their low latent heat of vaporization, exhibit complex behavior which mandates a detailed flow

physics study. The key objectives of this work are:

1. To assess the predictive capabilities of one-dimensional models for cryogenic cavitating venturis. Though simplified, 1D models provide valuable estimates of key flow parameters.

2. To develop two-dimensional models using ANSYS Fluent with appropriate cavitation models. Also to predict flow characteristics, such as cavitation length, and validate against experiments.

3. Design and develop a planar venturi test facility with flow visualization features. Conduct experiments using cryogenic liquid nitrogen to measure cavitation length and flow behavior. This study builds upon Wang and Brennen's approach [9], extending it to include thermal effects in cryogenic flows. Numerical simulations with 2D models provide a robust framework to capture the complex dynamics of cavitating venturi systems.

2 Numerical 1D model

In Brennen [9] model, the Rayleigh Plesset Equation for the isothermal case was assumed for solving the bubble dynamics. However, this bubble dynamics equation cannot be extended to the case of cryogenic liquids, as heat transfer effects are predominant in cryogenic liquids. It is advantageous to have an additional term in the same Brennen model [9] that accounts for heat transfer and extends to cryogenic cavitating venturi flows. The following section details models used for the Numerical 1D studies for cryogenic cavitating flows.

2.1 Derivation of modified Rayleigh-Plesset equation

The following derivation systematically introduces the thermal term into the Bubble dynamics equation. Starting from the classical form of the Rayleigh Plesset equation, the derivation for the modified Rayleigh Plesset equation is as follows

$$\left[R\ddot{R} + \frac{3}{2}\dot{R}^2 \right] = \frac{[P_\nu - P_\infty(t)]}{\rho_L} + \frac{P_{g0}}{\rho_L} \left[\frac{R_0}{R} \right]^{3\gamma} - \frac{2S}{\rho_L R} - \frac{4\mu \dot{R}}{\rho_L R} \quad (1)$$

The above is the simple Rayleigh-Plesset equation for the isothermal case. The equation does not have an appropriate term for handling the heat interactions. The vapour pressure inside the bubble can be represented as $P_\nu(T_B)$ in this equation. In an iso-thermal fluid such as water, there is no temperature difference between the bubble temperature T_B and the surrounding liquid temperature T_∞ . The above isothermal condition is an assumption which is not valid for cryogenic liquids as the slightest temperature difference between T_B and T_∞ causes a considerable change in the vapour pressure inside the bubble. The temperature gradient $T_\infty - T_B$ becomes a potential source for heat transfer influencing the bubble growth.

By small algebraic manipulation of adding and subtracting $P_\nu(T_\infty)$ in $[P_\nu(T_B) - P_\infty(t)]$ it can be written as

$$[P_\nu(T_B) - P_\infty(t)] = [P_\nu(T_\infty) - P_\infty(t)] + [P_\nu(T_B) - P_\nu(T_\infty)] \quad (2)$$

Substituting equation 2 in 1 the equation becomes of this form

$$\left[R\ddot{R} + \frac{3}{2}\dot{R}^2 \right] + \frac{2S}{\rho_L R} + \frac{4\mu \dot{R}}{\rho_L R} = \frac{P_{g0}}{\rho_L} \left[\frac{R_0}{R} \right]^{3\gamma} + \frac{[P_\nu(T_\infty) - P_\infty(t)]}{\rho_L} - \frac{[P_\nu(T_B) - P_\nu(T_\infty)]}{\rho_L} \quad (3)$$

The third term on the right-hand side of the equation is the thermal term, and the second term is the driving term for the bubble growth. To find an expression for the thermal term, we need to look into the heat Balance and B-factor theory [1] & [5]

The thermal effect in cryogenic liquids can be interpreted as the heat interaction between the vapour bubbles and the surrounding liquid. The production of a vapour volume V_ν requires the quantity of heat $\rho_\nu V_\nu L$ to be supplied (L is the latent heat of vaporization). This energy is given by the liquid near the vapour cavity. Hence, the liquid mass surrounding the vapour bubble gets cooled by supplying

heat to the bubble. Steffano [1] & [5] put forth a theory, popularly known as B-factor theory, which gives a non-dimensional number for temperature drop called B-factor [1]

The volume of liquid V_L after supplying the heat of vaporization reduces itself with its temperature by a drop ΔT , and the heat balance between the liquid and vapour is given by

$$\rho_\nu V_\nu L = \rho_l V_l C_{pl} \Delta T \quad (4)$$

From the above equation, the B-factor gives the ratio of the volume of vapour to that of the volume of liquid. Alternately, it is also given by the ratio of the actual temperature drop to the reference temperature drop, which is shown below

$$B = \frac{\Delta T}{\frac{\rho_\nu L}{\rho_l C_{pl}}} = \frac{V_\nu}{V_l} \quad (5)$$

Where,

$\Delta T^* = \frac{\rho_\nu L}{\rho_l C_{pl}}$ is the reference temperature drop and ΔT is the actual temperature drop.

This slight temperature drop ΔT in the liquid happens to be the reason for the difference in temperature between a vapour bubble and the liquid in the immediate vicinity, which affects the vapor pressure change inside the bubble, as the bubble temperature has now been slightly changed. If the drop in temperature is very small, then by Taylor series expansion, we can write

$$\Delta P_\nu = \frac{dP_\nu}{dT} \Delta T \quad (6)$$

The vapour pressure changes with respect to the temperature $\frac{dP_\nu}{dT}$ which is given by the Clausius Clayperon relation[8]

$$L = T \left[\frac{1}{\rho_\nu} - \frac{1}{\rho_l} \right] \frac{dP_\nu}{dT} \quad (7)$$

Usually, the liquid density ρ_l in the Clausius-Clapeyron relation is neglected, and the relation reduces to

$$L = \frac{T_\infty}{\rho_\nu} \frac{dP_\nu}{dT} \quad (8)$$

To estimate the temperature difference ΔT , the heat transfer between liquid and vapour bubble has to be quantified. In literature, both conductive and convective modes of heat transfer were assumed based on the flow conditions, i.e., if there is no slip between liquid and bubble, then the conductive approach is sufficient. But in our case, assuming a convective mode of heat transfer is applicable.

Assuming Q as the heat flux at the interface of bubble and liquid, then we can write

$$Q = hA\delta T \quad (9)$$

As this heat supplied by the liquid is the actual heat source for vapourization and growth of the bubble, a balance of heat can be done as shown below

$$h\delta T(4\pi R^2) = \frac{d}{dt} \left(\frac{4}{3}\pi R^3 \right) \rho_\nu L \quad (10)$$

Rearranging the equation in terms of δT gives,

$$\delta T = \frac{\rho_\nu L}{h} \dot{R} \quad (11)$$

Positive δT indicates a temperature decrement in liquid, but a temperature increment in vapour bubble. This, in turn, increases the vapour pressure inside the bubble, which in turn makes the bubble expand or grow. Similarly, it can be interpreted that the negative δT leads to shrinkage of the vapour bubble due to condensation.

Now, coming back to the thermal term as stated in equation 3, we can write

$$\frac{[P_\nu(T_B) - P_\nu(T_\infty)]}{\rho_L} = \frac{\delta P_\nu}{\rho_L}$$

substituting δP_ν from equation[25] gives

$$\frac{[P_\nu(T_B) - P_\nu(T_\infty)]}{\rho_L} = \frac{dP_\nu}{dT} \frac{\delta T}{\rho_L}$$

again δT can be substituted from equation[29] which results in an expression of thermal term as follows

$$\frac{[P_\nu(T_B) - P_\nu(T_\infty)]}{\rho_L} = \frac{dP_\nu}{dT} \frac{\rho_\nu L}{\rho_L} \frac{\dot{R}}{h} \quad (12)$$

After substituting equation[30] into [22] we finally get the **modified Rayleigh-Plesset** equation with thermal source term as follows

$$\left[R\ddot{R} + \frac{3}{2}\dot{R}^2 \right] + \frac{2S}{\rho_L R} + \frac{4\mu}{\rho_L} \frac{\dot{R}}{R} = \frac{P_{g0}}{\rho_L} \left[\frac{R_0}{R} \right]^{3\gamma} + \frac{[P_\nu(T_\infty) - P_\infty(t)]}{\rho} \frac{L}{L} - \frac{dP_\nu}{dT} \frac{\rho_\nu L}{\rho_L} \frac{\dot{R}}{h} \quad (13)$$

Equation 13 is the governing differential equation for bubble dynamics applicable for non-isothermal liquids such as cryogenic liquids.

2.2 Modelling 1D cavitating nozzle / Venturi flow

Similar to Wang and Brennen Quasi-1D model [9] for Bubbly Cavitating flows through a nozzle, a Quasi-1D model with thermal effects is attempted in this work applicable to cryogenic liquids. The continuity and momentum equations for bubbly two-phase flows along with the closures, i.e., the volume fraction equation and the modified Rayleigh Plesset equation along with the bubble momentum equation for estimation of bubble velocity, were considered in this model for solving bubble radius.

For modelling the heat transfer between bubble and liquid, a convective heat transfer model was taken from the existing Ranz and Marshall model [14]. The turbulence model was not incorporated in 1D numerical studies, as handling such equations would be tedious. Following assumptions were made in this model,

1. At any cross-section of the venturi, the bubbles had a uniform size, and the bubble number was assumed constant.
2. The bubble and the liquid temperatures were equal at the interface, and there was no friction or heat transfer between the venturi walls and the flowing fluid.
3. Liquid and vapour densities were assumed to be constant

Supposing that flow develops only in the longitudinal x direction, the steady bubbly flow continuity and momentum equations that Wang and Brennen used are given as follows

$$\frac{\partial(1-\alpha)A}{\partial t} + \frac{\partial(1-\alpha)Au}{\partial x} = 0$$

$$\frac{\partial u}{\partial t} + u \frac{\partial u}{\partial x} = -\frac{1}{2(1-\alpha)} \frac{C_p}{\partial x}$$

Where, $C_p(x, t) = \frac{(P(x, t) - P_0)}{(0.5\rho_l u_0^2)}$ is the fluid pressure coefficient $P(x, t)$ is the fluid pressure, P_0 is the upstream fluid pressure, u_0 is the upstream fluid velocity, and u is the velocity along the length of the profile. $A(x)$ corresponds to the area profile, which is the function of x (being a 1D case). The mathematical expression for the area profile $A(x)$ is

$$A(x) = \left\{ 1 - \frac{1}{2} C_{p,min} \left[1 - \cos \left(\frac{2\pi x}{L} \right) \right] \right\}^{-\frac{1}{2}} \quad (14)$$

$$\alpha(x, t) = \frac{\frac{4}{3}\pi\eta R(x, t)^3}{\left(1 + \frac{4}{3}\pi\eta R(x, t)^3\right)}$$

is the non-dimensional void fraction, $R(x, t)$ is the non-dimensional bubble radius, and η is the non-dimensional population number.

For modelling the non-linear bubble dynamics, a modified Rayleigh–Plesset equation 13 was used

$$\left[R\ddot{R} + \frac{3}{2}\dot{R}^2 \right] + \frac{2S}{\rho_L R} + \frac{4\mu}{\rho_L} \frac{\dot{R}}{R} = \frac{P_{g0}}{\rho_L} \left[\frac{R_0}{R} \right]^{3\gamma} + \frac{[P_\nu(T_\infty) - P_\infty(t)]}{\rho_L} - \frac{dP_\nu}{dT} \frac{\rho_\nu L}{\rho_L} \frac{\dot{R}}{h} \quad (15)$$

The above equation can be represented in total derivative form by replacing $\dot{R} = \frac{DR}{Dt}$, which is given by

$$\left[R \frac{D^2 R}{Dt^2} + \frac{3}{2} \left(\frac{DR}{Dt} \right)^2 \right] + \frac{2S}{\rho_l R} + \frac{4\nu_l DR}{R Dt} = \frac{P_{g0}}{\rho_l} \left[\frac{R_0}{R} \right]^{3\gamma} + \frac{[P_\nu(T_\infty) - P(x, t)]}{\rho_L} - \frac{dp_\nu}{dT} \frac{\rho_\nu L_{ev}}{\rho_L h_b} \frac{DR}{Dt} \quad (16)$$

In the above equation, the last term on the right side is the thermal term, and h_b is the convective heat transfer coefficient, which was modelled using the already existing Ranz and Marshall [14] model for the study of evaporation of droplets in spray drying which is given by

$$h_b = \frac{Nu_b K_l}{2R}$$

Where $Nu_b = 2 + 0.6Re_b^{\frac{1}{2}} Pr^{\frac{1}{3}}$ is the bubble Nusselt number, which in turn depends on the bubble Reynolds number (Re_b), and Prandtl number (Pr) which is given by [8] as

$$Re_b = 2R|\nu - u|/\lambda_l$$

$$Pr = \frac{C_{pl}\mu_l}{K_l}$$

where $\lambda_l = K_l/\rho C_p$ is the thermal diffusivity and K_l is the liquid thermal conductivity.

For solving bubble velocity, the bubble momentum equation formulated by Albagli et al. [13] was used, which is shown as follows

$$\rho_\nu \frac{D\nu}{Dt} + \frac{1}{2}\rho_l \left[\frac{D\nu}{Dt} - \frac{Du}{Dt} \right] = -\frac{\partial P(x, t)}{\partial x} - \frac{3}{8}\rho_l C_D \times \frac{(\nu - u)|\nu - u|}{R}$$

2.3 Wang and Brennen benchmark Results for Water with thermal term

A numerical 1D code using Matlab was written for solving the Brennen model with water as the fluid considering the effects of the thermal term. The results were plotted for the bubble radius, void fraction, coefficient of pressure, velocity of the liquid phase, and the growth contribution terms (thermal and pressure terms). The non-dimensional bubble radius, coefficient of pressure, void fraction, and non-dimensional void fraction plots are shown below in the figure 3,7, 8, 9 corresponds to the Rayleigh Plesset bubble dynamics equation with the thermal effects incorporated.

The superimposed plot of Wang and Brennen [9] bubble radius, coefficient of pressure, and void fraction plot with the current numerical model(with thermal effects) plot is shown in the figure 4,5,6

It can be inferred from the superimposed figures 4,5, 6 that there is no much variation in the bubble radius, void fraction, and coefficient fraction plot of current model and Brennen model [9]. However, deviations may be attributed to the additional thermal effect term. This indicated that including the thermal effect in the Rayleigh Plesset equation has no considerable role to play in the

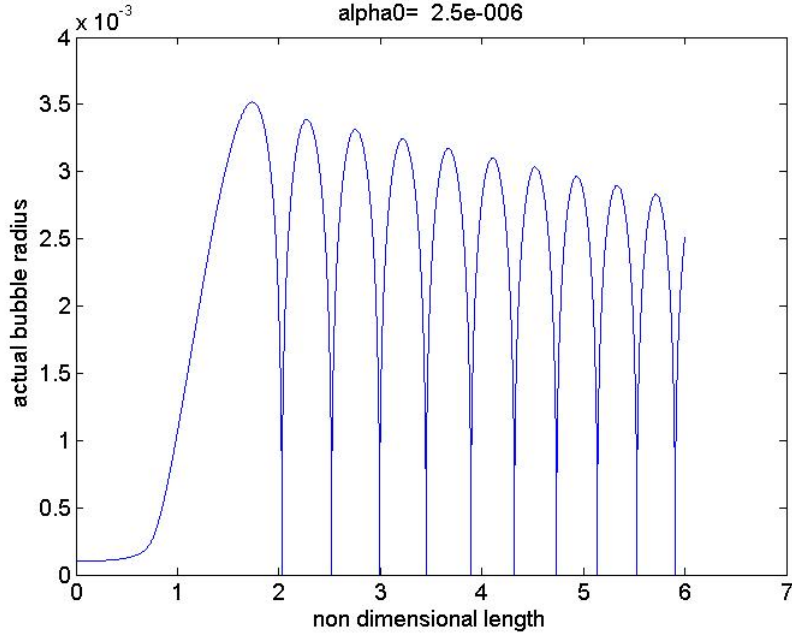


Figure 3: Non-dimensional Bubble radius plot for water at $\alpha_0 = 2.5 \times 10^{-6}$

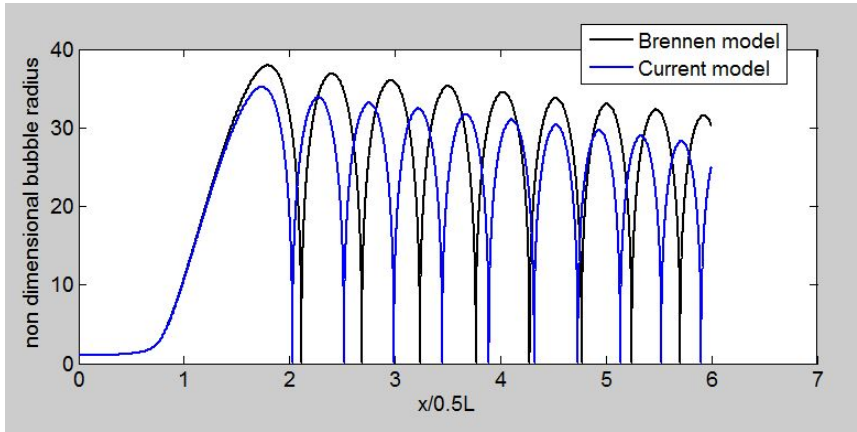


Figure 4: Non-Dimensional Bubble radius plot from Wang & Brennen [9] model and current model

bubble dynamics of Water. The reason for this is the minimal contribution of Thermal term in water.

The figure 10 gives the plot of source terms in the Rayleigh-Plesset equation. The thermal source term is compared with a pressure source term. The values of the same are plotted for an initial void fraction of $\alpha_0 = 2.5 \times 10^{-6}$, where the term α_0 is the initial void fraction which has been arbitrarily assumed in the Wang and Brennen model [9]. This initial void fraction significantly impacts the numerical prediction of bubble radius as this signifies the number of nucleation sites or microscopic voids in the liquid phase.

For understanding the domination of different source terms in the bubble dynamics, the right-hand side of the modified Rayleigh-Plesset equation containing such source terms was handled separately, and the magnitude of the same were plotted. i.e., all other terms except the thermal term were taken as the pressure source term. The following figure 10,11 shows the contribution of the above-mentioned thermal term and pressure term.

It can be inferred from the plots that the contribution of the thermal term within the flow domain of the venturi is small and is of the order 10^{-1} when compared to the contribution from the pressure term, which is of the order 10^4 . This points out to the fact that the explicit modelling of the thermal term in the modified Rayleigh Plesset Equation may not provide pronounced effects for fluids with the high latent heat of vapourization. This fact explains the close prediction of the Wang & Brennen

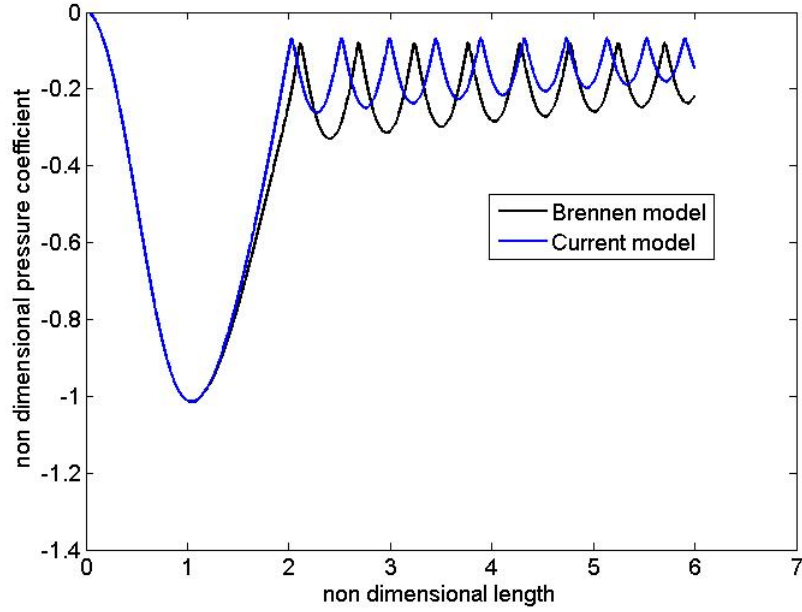


Figure 5: Coefficient of Pressure plot from Wang & Brennen [9] model and current model

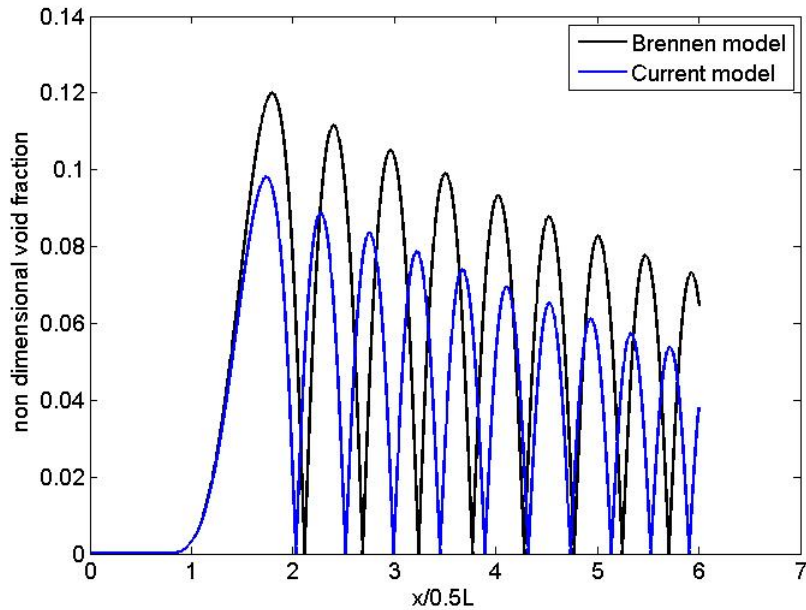


Figure 6: Void fraction plot from Wang & Brennen [9] model and current model

model results , where such a thermal term is not modelled.

Having benchmarked the model, the same model is now extended to predict cavitating flows of liquid nitrogen.

However, the present one-dimensional model is far from providing estimates for performance prediction of cavitating venturi, and more systematic work in developing proper mathematical models to predict the performance would be required. Hence, a systematic study of a simple planar 2D numerical study was attempted using ANSYS fluent, which will be discussed.

2.4 Numerical 1D Results: for the present case

The numerical 1D simulation was done for liquid nitrogen, including the thermal effect, using the modified Rayleigh Plesset equation using MATLAB.

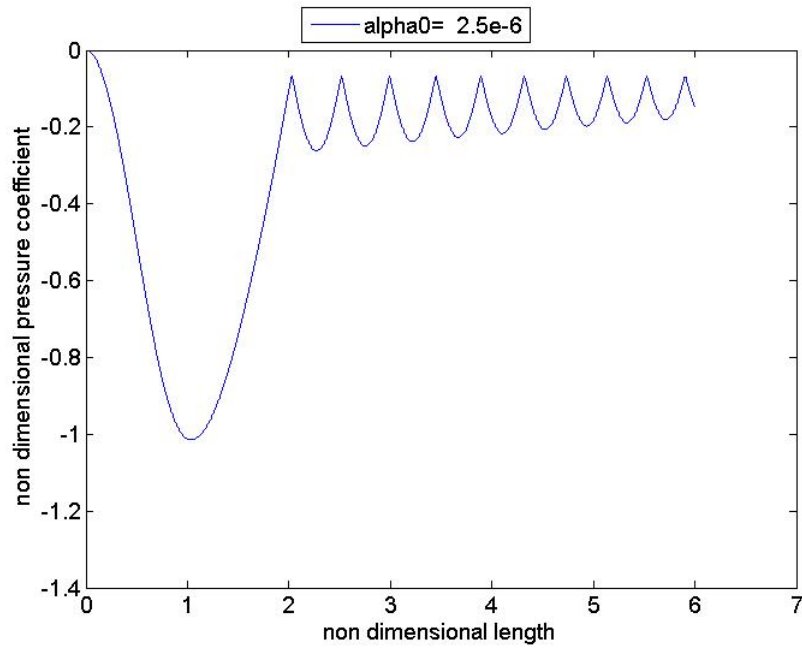


Figure 7: Coefficient of Pressure plot for water at $\alpha_0 = 2.5 \times 10^{-6}$

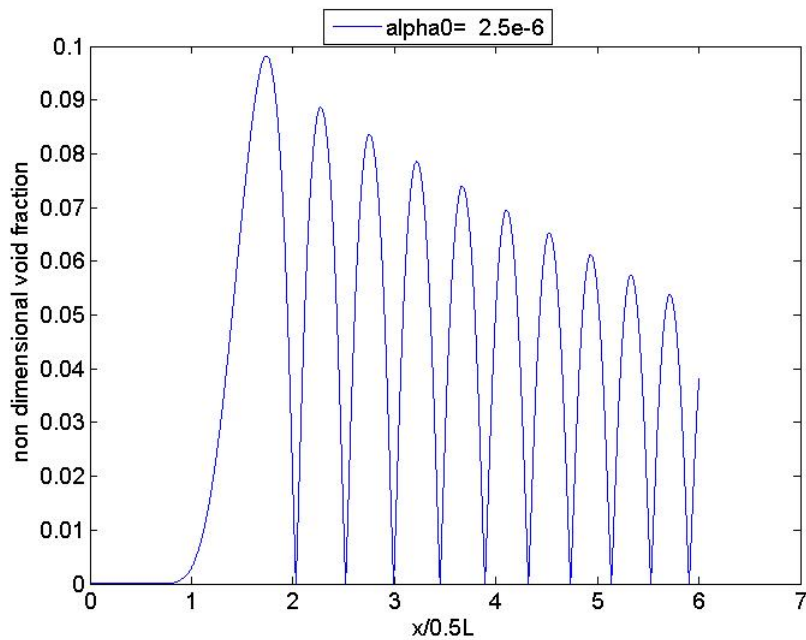


Figure 8: Void fraction plot for water at $\alpha_0 = 2.5 \times 10^{-6}$

Bubble radius, coefficient of pressure, and void fraction were plotted for different cases. Since the numerical model is an initial value problem, the initial values were assumed for all the variables in line with Wang and Brennen [9] model. It was inferred that the initial void fraction had a considerable effect on the nature of the solution.

2.5 1D Numerical Test cases

2.5.1 Case-1

For an Initial void fraction $\alpha_0 = 2.5 \times 10^{-6}$ and $C_p=0$

From the figure 12,13, it is evident that the non-dimensional bubble radius grows along the con-

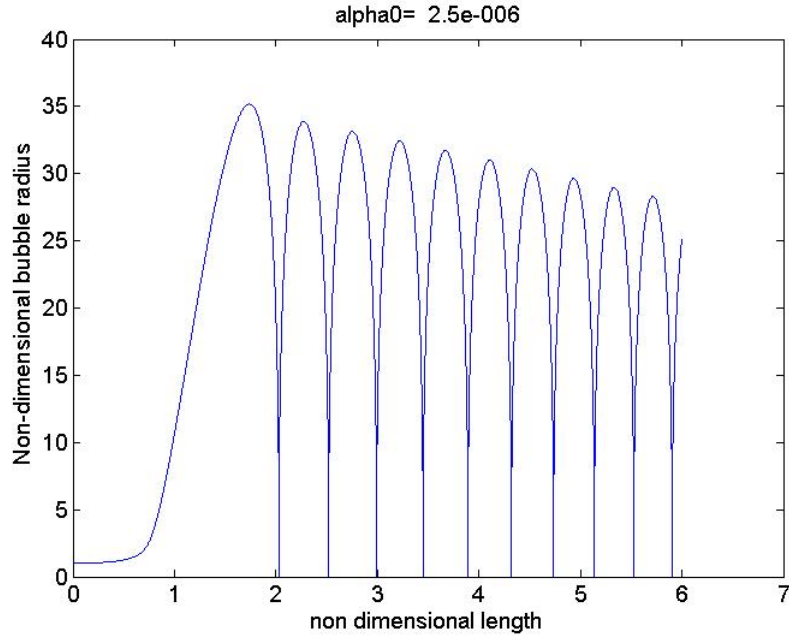


Figure 9: Non-dimensional bubble radius plot for water at $\alpha_0 = 2.5 \times 10^{-6}$

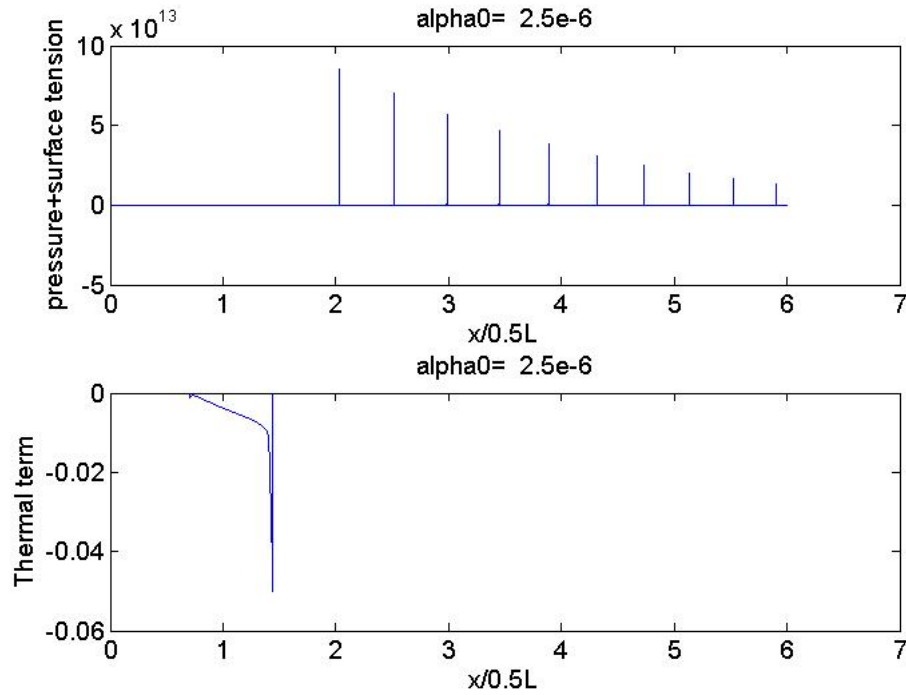


Figure 10: Source term plots for water at $\alpha_0 = 2.5 \times 10^{-6}$

verging section from 1 to 3.4 up to the throat ($x = 0$ indicates the beginning of the converging section as per Brennen Area profile, $x = 1$ indicates the throat section (or) beginning of the diverging section and $x = 2$ indicates the exit of diverging section), and dampens from the throat to the initial value of 1 at the exit of the nozzle and the region away from the nozzle exit.

The void fraction plot, as shown in figure 14, increases continuously up to 3.8×10^{-4} after the nozzle exits from the location of 2.7 to the far downstream of the nozzle to reach the value of 1 which corresponds to fully vapour condition. From the plot for the coefficient of pressure shown in the figure 15, the same behaviour is inferred.

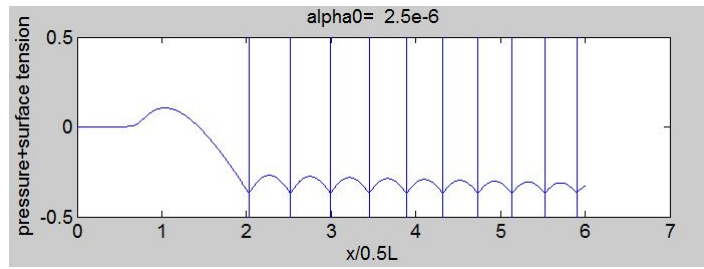


Figure 11: Magnified view of pressure source term plots for water at $\alpha_0 = 2.5 \times 10^{-6}$

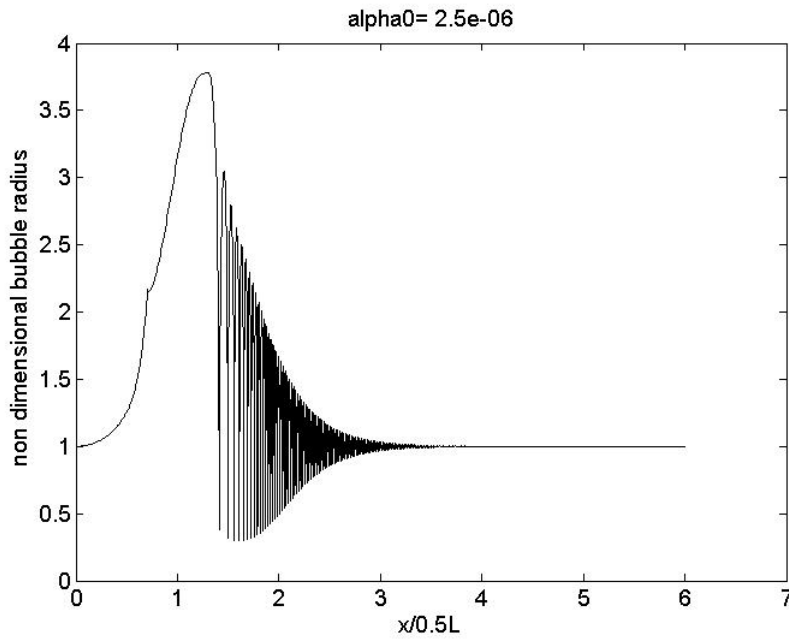


Figure 12: Non-dimensional bubble radius plot for case 1 of Liquid Nitrogen

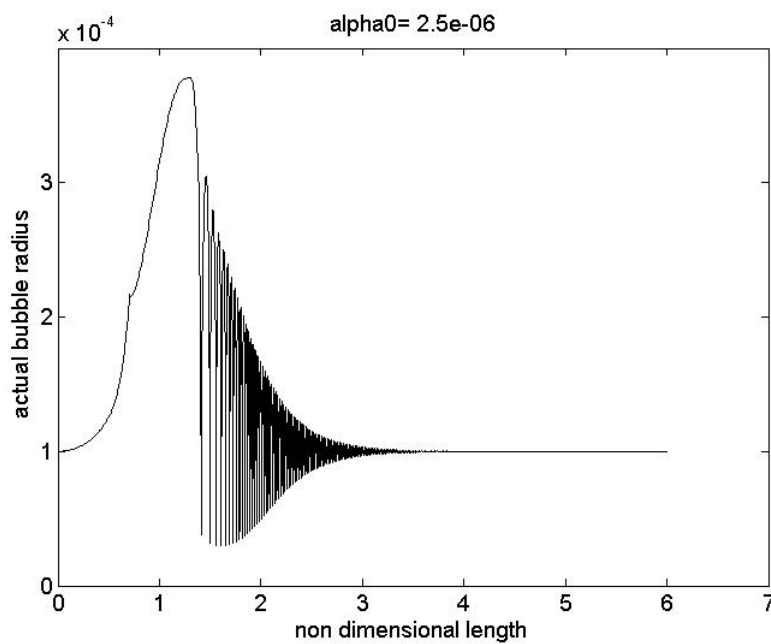


Figure 13: Actual bubble radius plot for case 1 of Liquid Nitrogen

The magnitude of Pressure and Thermal source term is shown as follows, which shows that the

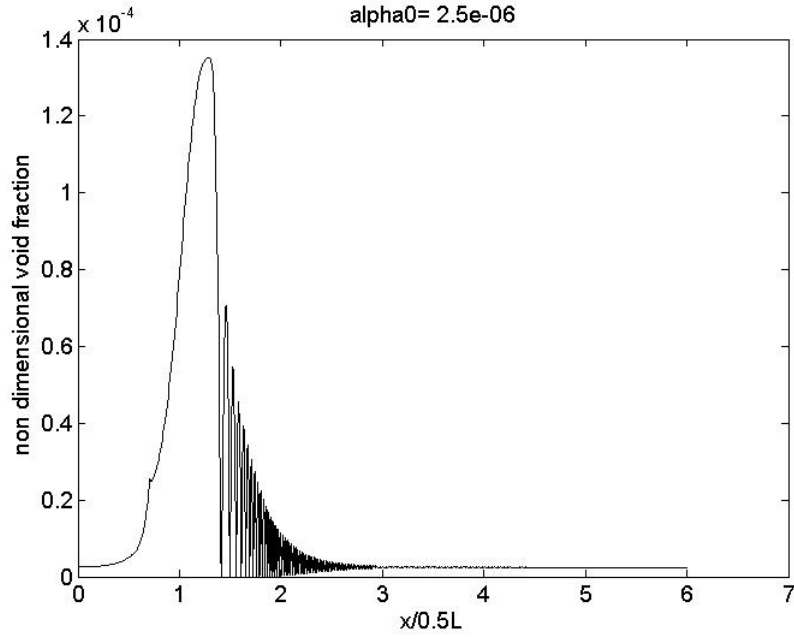


Figure 14: Non dimensional Void fraction plot for the case1 of Liquid nitrogen

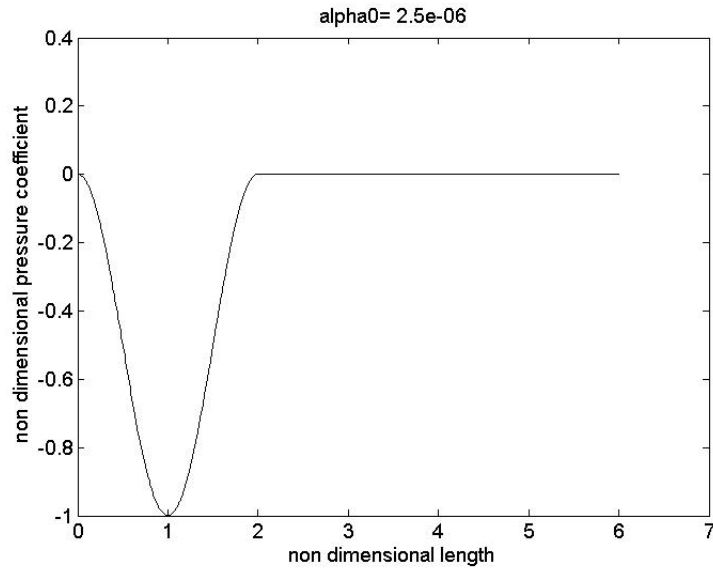


Figure 15: Coefficient of Pressure plot for the case 1 of Liquid nitrogen

magnitude of the thermal term for liquid nitrogen is 10 times the same for water, The magnitude of Pressure and Thermal source term is shown as follows, which shows that the magnitude of the thermal term for liquid nitrogen is 10 times the same for water, indicating the domination of thermal term in cryogenic liquids compared with isothermal fluids such as water 17. The following figures 17, 18 shows the source terms plotted for case1

2.5.2 Case-2

Plot for the same are predicted for an Initial void fraction of $\alpha_0 = 3.1 \times 10^{-6}$ and coefficient of pressure $C_p=0$

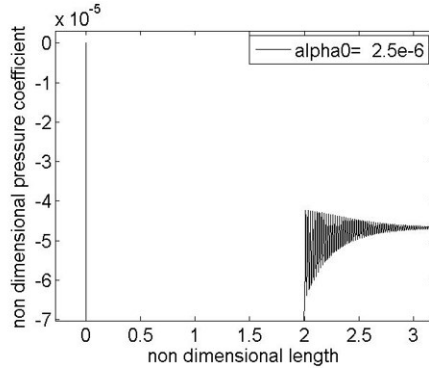


Figure 16: Magnified view of coefficient of Pressure plot for case 1 of Liquid nitrogen

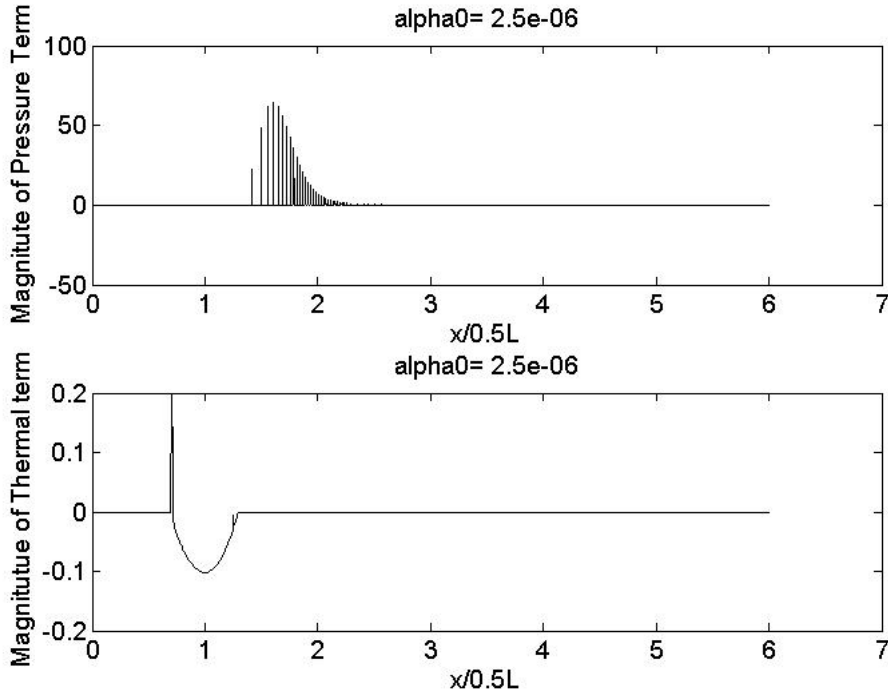


Figure 17: Magnitude of Pressure and Thermal source term plot

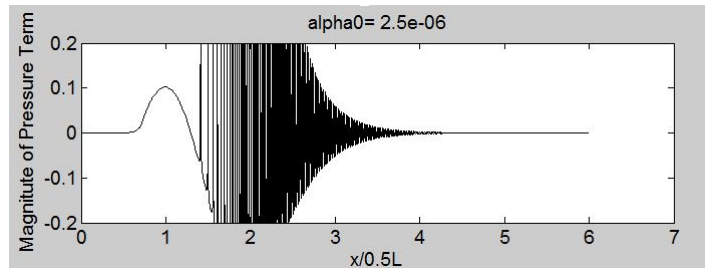


Figure 18: Magnified view of pressure source term

2.5.3 Case-3

Plot for the same is predicted for an Initial void fraction of $\alpha_0 = 3.0 \times 10^{-6}$ and coefficient of pressure $C_p = 0$

The 1D numerical model for cavitating flows with the thermal effects resulted in successful benchmarking of the Wang & Brennen [9] solution for water. The extension of the same model for cryogenic cavitating nozzle flows resulted in the damping solutions as the behaviour of cryogenic liquid nitrogen distinctly differs from the water. Overall, it can be ascertained that the 1D numerical model had

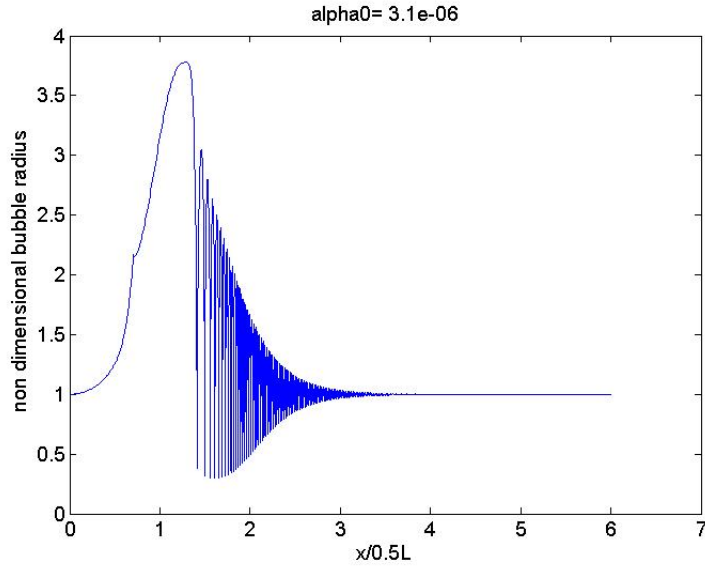


Figure 19: Non-dimensional bubble radius plot for the case-2 of Liquid Nitrogen

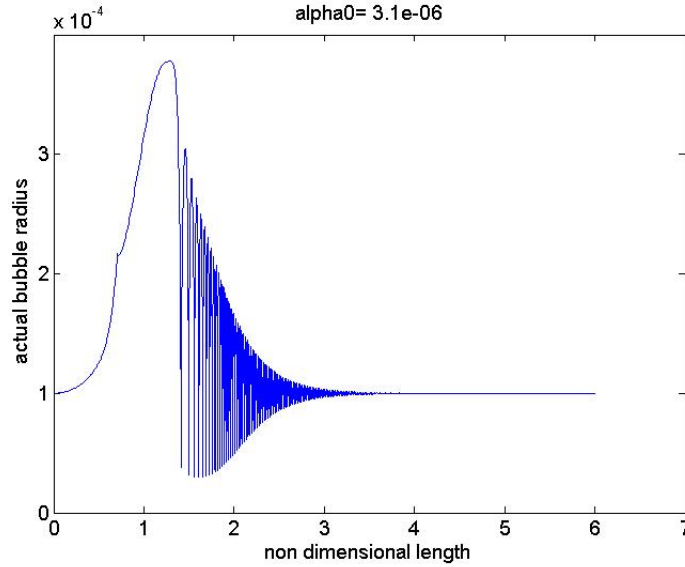


Figure 20: Actual bubble radius plot for case 2 of Liquid Nitrogen

limited predictability of the nature of cavitating flows, which are restricted to bubble radius, void fractions, coefficient of pressure, and the thermal and pressure source terms corresponding to a single bubble as the governing Rayleigh Plesset equation itself is valid for dynamics of the single bubble only. However, cavitation is a cluster phenomenon that demands the extension of the studies to two-dimensional numerical and experimental studies, whose attempted results are given in the subsequent sections.

3 Two-dimensional model CFD Studies

The following section systematically starts with an overview of the methodology adopted for 2D numerical studies using the commercial CFD solver ANSYS Fluent. The simulations have been carried out to capture the cavitating flows in a Venturi profile chosen to be symmetric, with a turbulence model to get insight into the actual experimental work. Simulations were done for cryogenic liquid nitrogen. The governing equations, such as continuity and momentum equations for the multiphase model, are solved using finite volume fluent code. Here, we discuss the viscous modeling, interfacial effects,

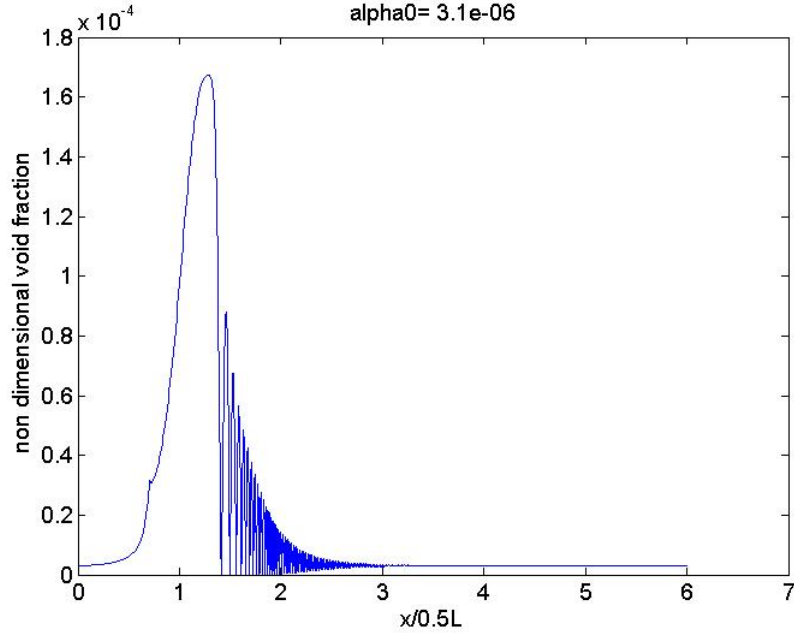


Figure 21: Non-dimensional Void fraction plot for the case 2 of Liquid nitrogen

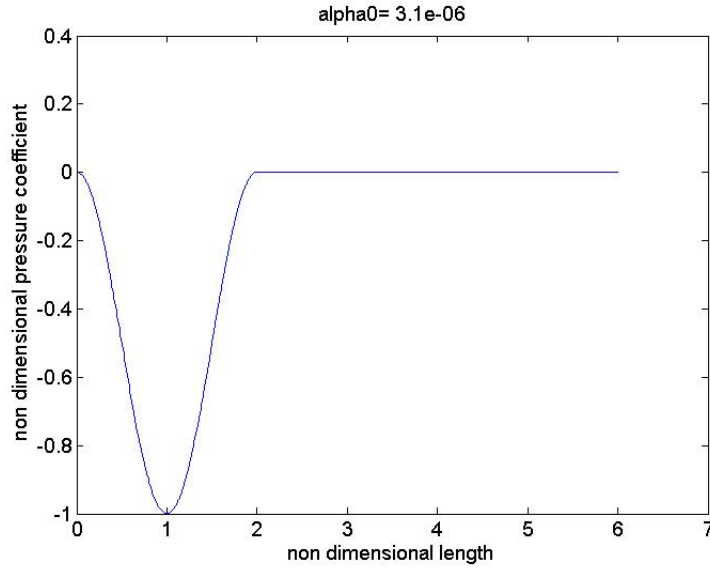


Figure 22: Coefficient of Pressure plot for the case 2 of Liquid nitrogen

solution methodology, and the boundary conditions used for the benchmarking test case of Hord et al. [5] and the extension of the same for current 2D numerical work.

3.1 Turbulence Modelling

The actual cavitating nozzle and venturi flows are turbulent in nature. Hence, a standard turbulence model has been incorporated into the simulations. Realizable $k-\varepsilon$ was used in simulations. The chosen model of $k-\varepsilon$ is in line with the internal flows, and the coefficients for the same are the standard values built into the ANSYS-fluent. The model has two transport equations, one for turbulent kinetic energy k and another for turbulent dissipation ε . The two transport equations are given as follows

$$\frac{\partial}{\partial t}(\rho k) + \frac{\partial}{\partial x_i}(\rho k u_i) = \frac{\partial}{\partial x_j} \left[\left(\mu + \frac{\mu_t}{\sigma_k} \right) \frac{\partial k}{\partial x_j} \right] + G_k + G_b - \rho \varepsilon - Y_m \quad (17)$$

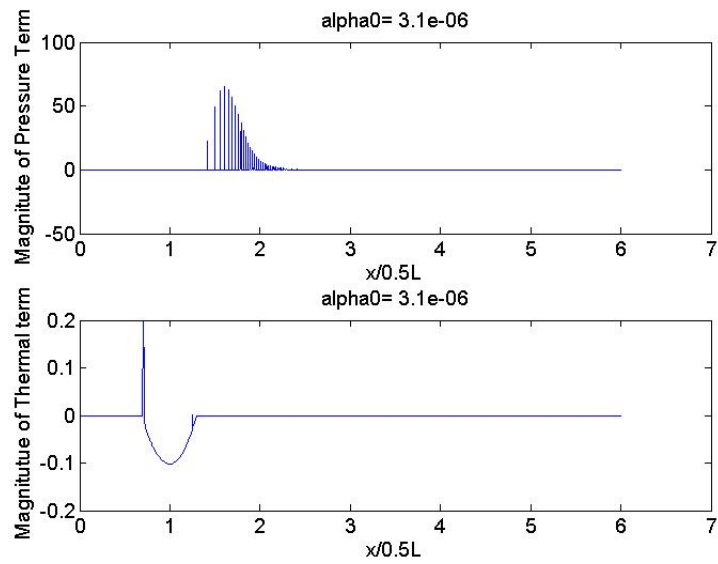


Figure 23: Magnitude of Pressure and Thermal source term plot

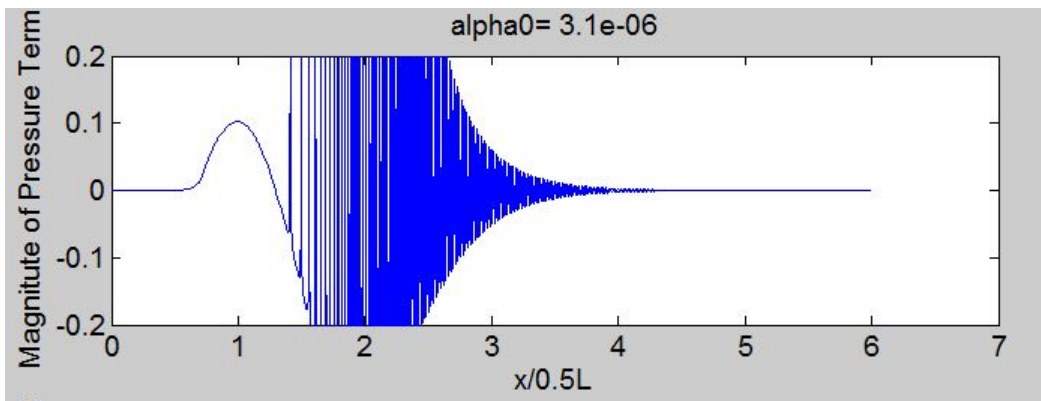


Figure 24: Magnified view of pressure source term

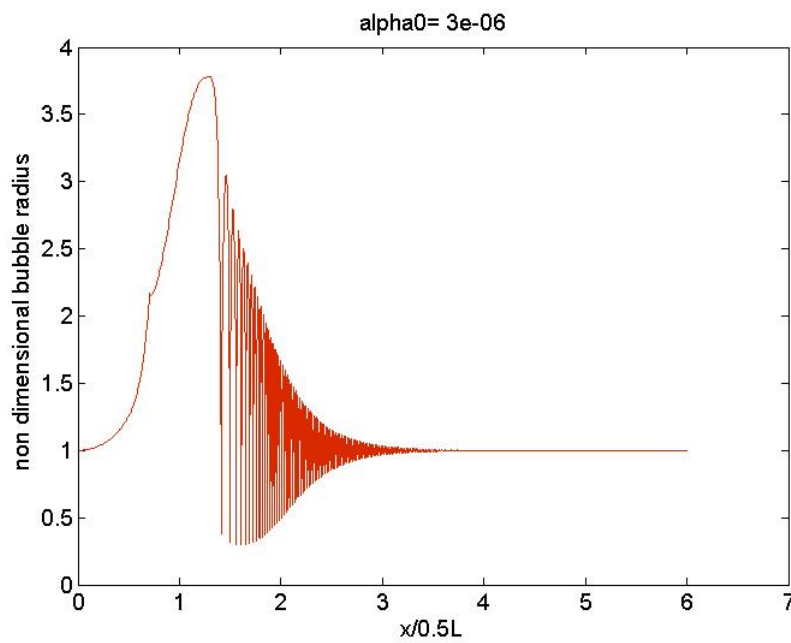


Figure 25: Non-dimensional bubble radius plot for the case 3 of Liquid Nitrogen

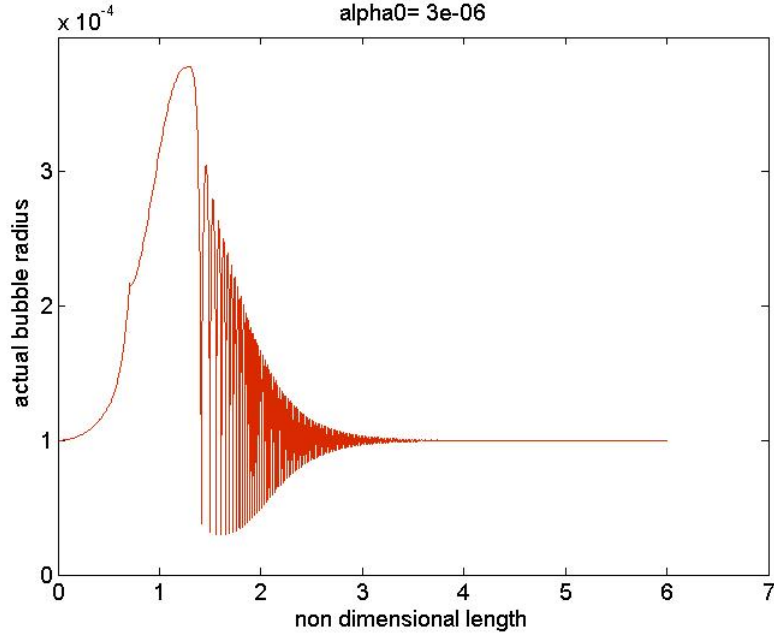


Figure 26: Actual bubble radius plot for case 3 of Liquid Nitrogen

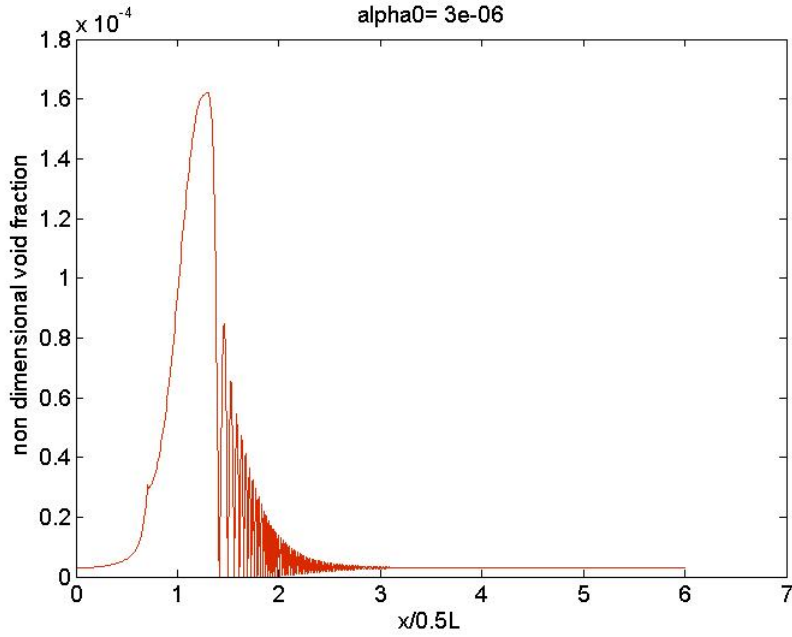


Figure 27: Non-dimensional Void fraction plot for the case 3 of Liquid nitrogen

And

$$\frac{\partial}{\partial t}(\rho\varepsilon) + \frac{\partial}{\partial x_i}(\rho\varepsilon u_i) = \frac{\partial}{\partial x_j} \left[\left(\mu + \frac{\mu_t}{\sigma_\varepsilon} \right) \frac{\partial \varepsilon}{\partial x_j} \right] + \rho C_1 S_l \varepsilon + C_{1\varepsilon} \frac{\varepsilon}{k} (G_k + C_{3\varepsilon b} G_b) - C_{2\varepsilon} \rho \frac{\varepsilon^2}{k + \sqrt{\nu \varepsilon}} \quad (18)$$

Where, $C_1 = \max \left[0.43 + \frac{\eta}{\eta+5} \right]$, $\eta = \frac{S_l k}{\varepsilon}$, $S_l = \sqrt{2 S_{ij} S_{ij}}$ is the modulus of mean strain rate tensor.

The turbulent viscosity $\mu_t = \rho C_\mu \frac{k^2}{\varepsilon}$, where C_μ is a function of mean strain rate, the angular velocity of the system rotation, and the turbulence fields such as k and ε . The model constants are

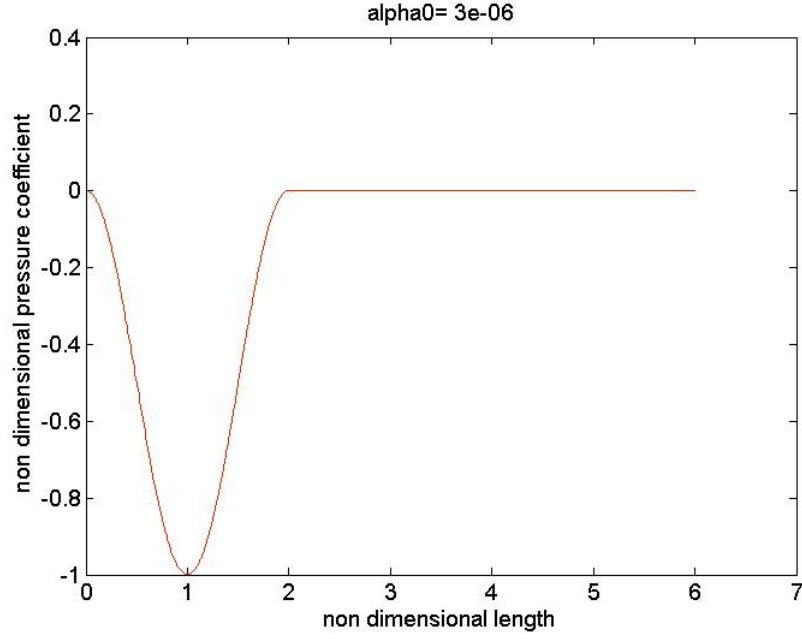


Figure 28: Coefficient of Pressure plot for the case 3 of Liquid nitrogen

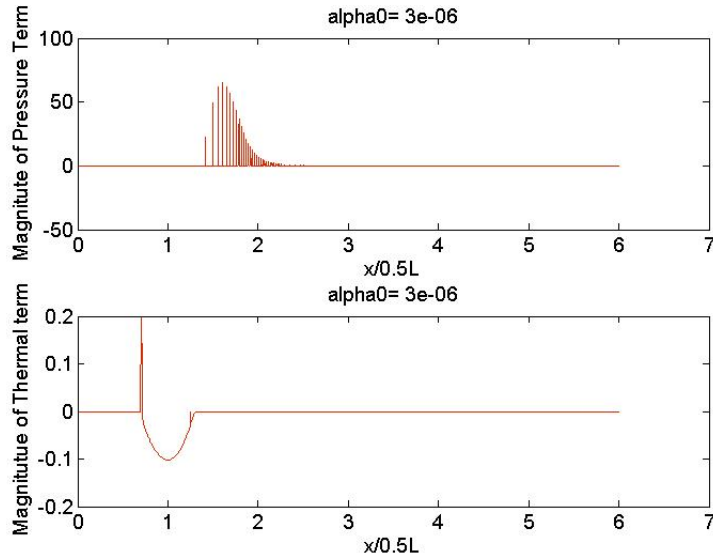


Figure 29: Magnitude of Pressure and Thermal source term plot

given by,

$$C_{1\varepsilon} = 1.44, \quad C_{2\varepsilon} = 1.9, \quad \sigma_k = 1, \quad \sigma_\varepsilon = 1.2$$

The term G_k indicates the production of turbulent kinetic energy and is given by,

$$G_k = \mu_t S_l^2$$

The turbulence production due to buoyancy forces can be computed from the following relation

$$G_b = \beta_g \frac{\mu_t}{Pr_t} \frac{\partial T}{\partial x_i}$$

3.2 Modelling Interfacial effects

3.2.1 Schnerr Sauer model for Mass Transfer

Estimation of mass transfer between the two phases has to be taken care of for complete cavitation modelling. The Schnerr and Sauer model addresses the net mass transfer from the liquid to the vapour. The vapour transport equation is given by

$$\frac{\partial}{\partial t}(\alpha\rho_\nu) + \nabla \cdot (\alpha\rho_\nu \vec{v}) = \frac{\rho_\nu \rho_l}{\rho} \frac{D\alpha}{Dt}$$

The net source term for mass is given by the right side of the above equation as follows

$$\dot{m} = \frac{\rho_\nu \rho_l}{\rho} \frac{D\alpha}{Dt}$$

Schnerr-Sauer model incorporated an expression that relates the vapour volume fraction to the bubble number per unit volume of liquid, which is defined as

$$\alpha = \frac{\eta_b \frac{4}{3} \pi R_b^3}{1 + \eta_b \frac{4}{3} \pi R_b^3}$$

R_b is the bubble radius, and η_b is the bubble population number per unit volume of the liquid. This model assumes that the number of bubbles is neither created nor destroyed. To model bubble dynamics, the Rayleigh-Plesset equation in simple form was incorporated that was built with Schnerr-Sauer model, which is given by

$$\frac{D\alpha}{Dt} = \sqrt{\frac{(P_b - P)^2}{\rho_l^3}} \quad (19)$$

Where P_b is the bubble pressure, P is the pressure, far away from the bubble. Using the above relations, the mass source term is

$$\dot{m} = \frac{\rho_\nu \rho_l}{\rho} \alpha(1 - \alpha) \frac{3}{R_b} \sqrt{\frac{(P_b - P)^2}{\rho_l^3}}$$

3.3 Interfacial Heat Transfer Effects

Modelling the convective heat transfer coefficient h_b was given by Ranz and Marshall [14] model, which is inbuilt in Fluent and is given as follows

$$h_b = h_{pq} = \frac{6k_q \alpha_p \alpha_q Nu_p}{d_p^2}$$

Here k_q is the thermal conductivity of the q^{th} face. The Nusselt number was determined from

$$Nu_p = 2.0 + 0.6 Re_p^{1/2} Pr^{1/3}$$

Where Re_p is the Reynolds number of the p^{th} phase and Pr is the Prandtl number of the q^{th} phase.

3.4 Benchmark of 2D simulations with experimental work of Hord et al.

An attempt was made to benchmark the 2D numerical work with the experimental test case of Hord 121B [5] for validating the cavitating length for liquid hydrogen flows in a venturi profile.

A finite-volume mesh using Ansys workbench was performed for the actual venturi profile used by Hord. A grid independence study was done for the venturi, and a grid-independent solution was obtained for a mesh with 51,335 nodes and 50527 elements. The following figure shows the meshed model of the venturi profile.

The simulation was done with the boundary conditions taken from the experimental data of Hord et al. [5].

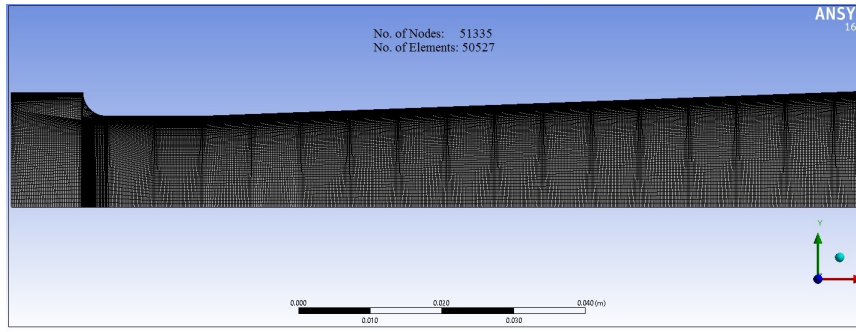


Figure 30: Mesh details of Hord experimental venturi profile

3.4.1 Solution Methodology

The simulations were performed using fluent with the Eulerian multiphase model. An implicit finite-volume scheme is based on a segregated pressure-based solver with SIMPLE as the pressure-velocity coupling. A second-order upwind scheme was used for continuity, momentum, energy, turbulent dissipation, and kinetic energy.

Being turbulent flow, the wall y^+ was assumed to be 30, and the resolution of grid element size near the boundary was 2×10^{-04} m. A default standard wall function was chosen for solution methodology [8].

The residuals were set to 0.00001 for continuity, velocity, K, and ϵ . For the energy equation and volume fraction, the residuals were set to be 1^{-06} .

Following are the simulation results for the contour of Vapour fraction obtained using Ansys fluent

3.4.2 Simulation Results

The following table31 is the actual experimental result of Hord for various test cases from the flow visualization study.

Test Case	Inlet Temperature T_0 (K)	Inlet Velocity V_0 (m/s)	Inlet Pressure P_0 (N/Cm ²)	Cavitating Length (cm)
121B	22.77	32.3	23.20	8.26
124B	22.81	31.8	23.09	8.26
128B	22.40	51.3	29.43	8.89
132A	22.49	57.2	38.40	3.18

Figure 31: Table showing experimental test cases of Hord

The following figure32 shows the simulation results of Hord test case 121B. The blue fill indicates the complete liquid phase, and the red fill indicates the complete vapour phase.

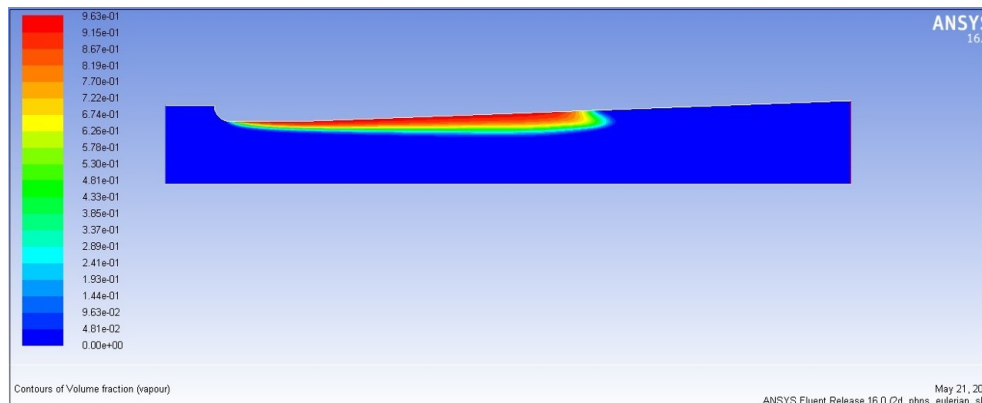


Figure 32: Contour of volume fraction from the simulation results of Hord profile

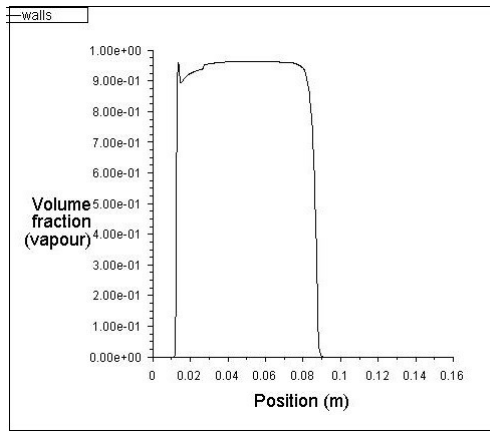


Figure 33: Plot for volume fraction as a function profile length

From the vapour volume fraction plot33, it is evident that the vapour phase dominates in the cavitating regime, and the plot shows the cavitating length of 0.085 m or 8.5 cm.

The simulation results for other test cases are as follows:

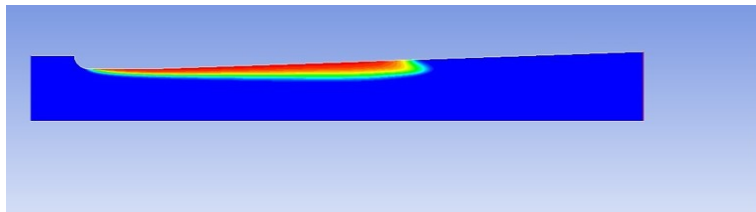


Figure 34: Contour of volume fraction for test case 124B



Figure 35: Contour of volume fraction for test case 126A

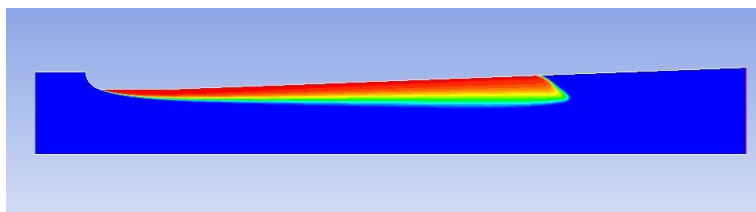


Figure 36: Contour of volume fraction for test case 128A

3.4.3 Estimating Cavitating length

The details of the measured Cavitating length from the contour of the void fraction is shown in the below figure37

In the above figure, the cavitating length indicates the domination of vapour phase. The simulation result for a sample case, as shown in the figure37 indicated a Cavitating Length of 9.13 cm against the actual 8.89 cm of experimental cavitating length for test case 128B measured by Hord et al. [5]. Exact matching of simulation and experimental data was impossible as the solutions are independent

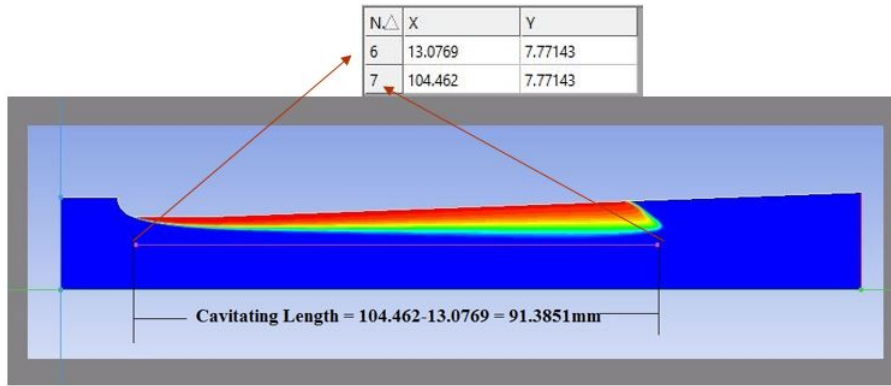


Figure 37: Cavitation length measurement details

of numerical solution methodology and wall treatments. Still, the computation results closely match the experimental result of Hord et al. [5]. as the error in prediction is less than 4%.

Error prediction in cavitating length against the actual experimental length for different test cases are shown in the figure38 containing the table Similar work was done by Rodio et al. [8], and the

Test Case	Experimental Cavitating Length (cm)	Simulation Cavitating Length (cm)	Error (%) in cavitation length
121B	8.26	8.5343	3.3%
124B	8.26	8.5340	3.3%
128B	8.89	9.138	2.78%
132A	3.18	3.05	4.0%

Figure 38: Table showing error in the simulation results of Hord

contour of the void fraction of the vapour obtained for the Hord test case 121B [5] is shown in the following figure.

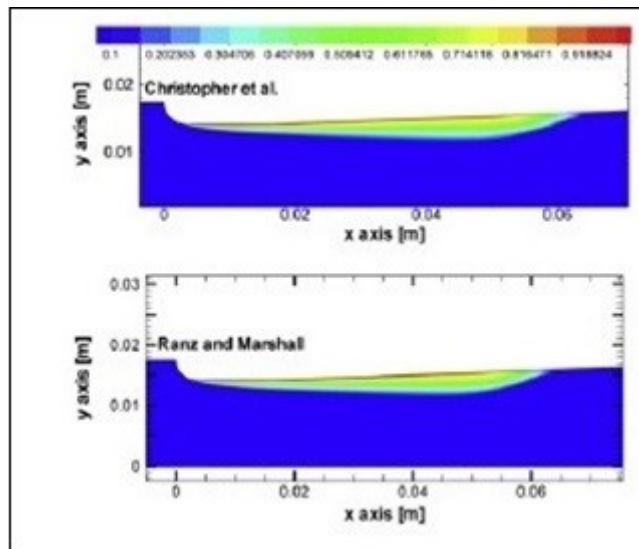


Figure 39: Contours of the void fraction obtained by Rodio et.al [8] for Hord test case 121B [5]

It was observed that the simulation results by Rodio et al. [8] overpredicts the experimental cavitating length observed by Hord et al. [5]. The following measurement proofs validate the above interpretation of the result.

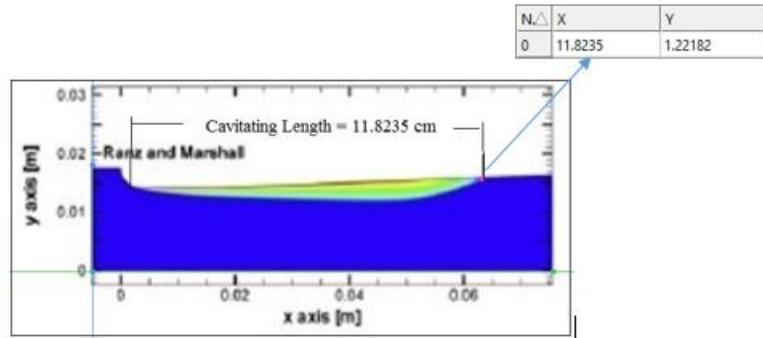


Figure 40: Cavitation Length measurement details for Rodio et.al [8] work

The calculated cavitating length from the above contours of volume fraction gives a length of 11.8235 cm compared to the actual experimental cavitating length of 8.26 cm, measured by Hord et al. [5]. However, the wrong prediction of cavitation length may not be precisely due to the model used, as mesh methods and chosen wall functions have significant influences on the convergence of numerical solution. Having benchmarked the 2D numerical model for cryogenic cavitating venturi with Hord et al. [5] experimental test cases for predicting the cavitating length in the venturi profile. The same is now extended for the current work, the details of which are given in the following section.

4 2D simulation for Current Work

4.1 Computational Model Details

A steady-state, two-dimensional, incompressible, turbulent Eulerian mixture model was developed based on finite-volume formulation. The details of the computational model are shown below

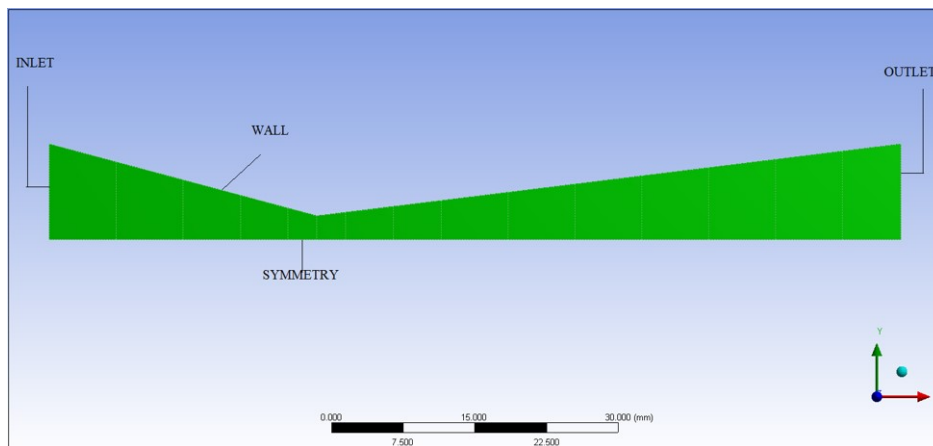


Figure 41: Computation model with domain or boundary

The figure41depicts the actual 2D model of the venturi region of the test section developed for simulations. The dimensions correspond to the actual dimensions of the experimental setup. The boundaries include an inlet, wall, symmetry, and the outlet.

Domain discretization or meshing was done with Ansys and Pointwise. The entire domain was discretized using structural quadrilateral elements. The wall y^+ requirement for $k - \epsilon$ model was assumed to be around 30 and accordingly the thickness of the first computational grid was fixed.

4.2 Boundary conditions

The entire domain was divided into three regions: inlet, outlet, and walls. Only the inlet and outlet boundary conditions were found to be very important as they play a very significant role in the convergence of solutions.

The inlet and outlet pressure conditions from the experiments were used as boundary conditions, with the inlet temperature assumed as 77 K for the liquid phase of liquid nitrogen. Also, the inlet vapour fraction is given 0 as the inlet condition is fully liquid.

Adiabatic wall boundary conditions were given as there were no assumptions of heat transfer effects between the wall boundary and fluid.

The outlet boundary condition was atmospheric pressure, as the experiment's venturi profile opens to the atmosphere. Liquid temperature condition at the outlet is assumed to be 77 K, and vapour fraction at the outlet is assumed to be 0 indicating a single-phase liquid.

4.3 Solution Methodology

The same solution methodology was used for the Hord benchmark simulation. It is the exact segregated pressure-based solver with SIMPLE as the pressure-velocity coupling. A second-order upwind scheme was used for continuity, momentum, energy, turbulent dissipation, and kinetic energy.

under-relaxation parameters for vapourization mass were set to 0.5, and the volume fraction was set to 0.95.

The residuals were set to be 0.001 for continuity, velocity, K , and ε . For Energy and volume fraction, the residuals were set to be 1 e^{-06} . The simulation results for the contour of vapour fraction obtained using Ansys fluent are discussed in following section.

4.4 Grid Independence

A grid independence study was carried out to find the optimum number of grid points that ensures correct capturing of flow characteristics and ensures that the solution does not change with further increase in the number of grid points.

The domain was discretized using finite volume meshing in Ansys with grid elements of 8346, 40926, and 102482 elements. It was found that a grid-independent solution was obtained with a mesh of 40926 grid elements. The following picture shows the meshing details. For near-wall treatment, a default wall $y^+ > 30$ for turbulent flow was assumed, and accordingly, the size of the first grid element near the wall was chosen for meshing. The following picture shows the meshing details

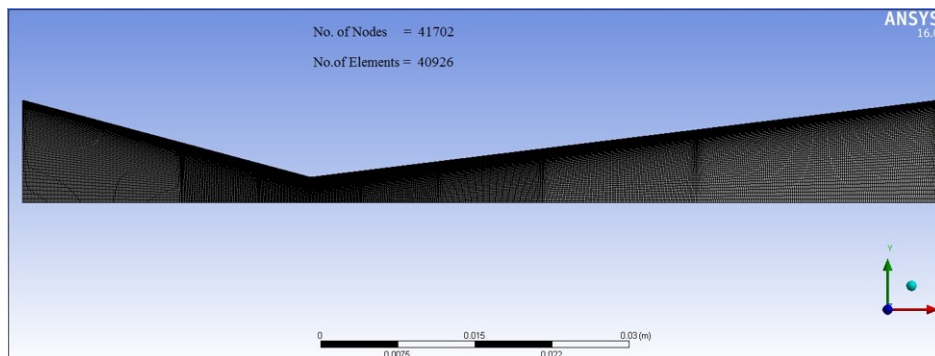


Figure 42: Mesh detail for the venturi

4.5 2D Numerical results

This section discusses the simulation results of the symmetric venturi corresponding to 40926 grid elements. The Boundary conditions used in the simulations were in line with experimental observations.

4.5.1 Boundary Conditions

The following table 43 gives the details of the experimental observations. The same values of pressure are used for 2D simulations as boundary conditions.

Test Case Scan Data	Inlet Pressure P_1 (bar)	Downstream Pressure P_2 (bar)	Pressure Ratio P_2/P_1	Experimental Cavitating Length (cm)
396	1.2347	0.999989	0.809905	4.3826
397	1.2345	1.000079	0.810109	4.3826
398	1.2344	0.999956	0.810075	4.38255
399	1.2343	0.999833	0.810041	4.38255

Figure 43: Table showing experimental data

The simulation results obtained from Ansys-Fluent for various test cases are as follows.

4.5.2 Contour of Volume fraction(Liquid)

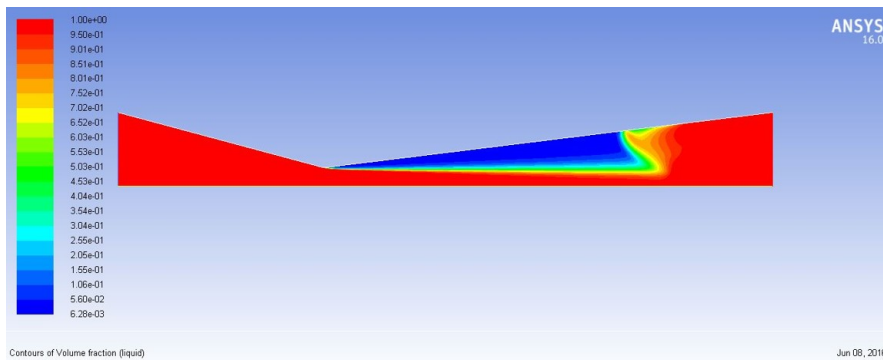


Figure 44: Contours of volume fraction for test case 396

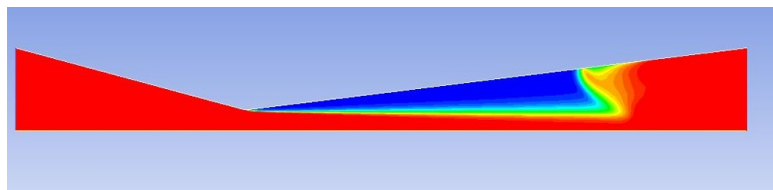


Figure 45: Contours of volume fraction for test case 397

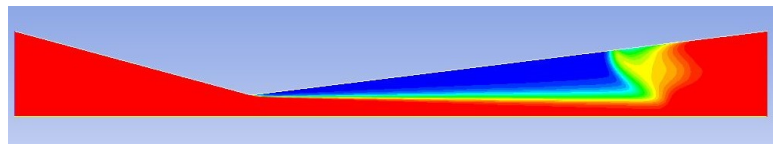


Figure 46: Contours of volume fraction for test case 398

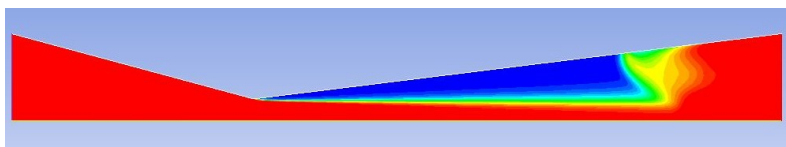


Figure 47: Contours of volume fraction for test case 399

The blue fill indicates a complete vapour phase, and the red fill indicates a fully liquid phase. The yellow region corresponds to a vapour fraction of 0.6, which indicates a thin two-phase regime, which is a point where the vapour is ready to convert back to the single-phase liquid. It is evident from the above figures that there is a distinct cavitation regime from the throat section up to a certain length in the downstream section of the venturi that corresponds to the cavitating length of the venturi.

4.5.3 Cavitating Length Measurement

The sample calculation of the cavitating length is shown as follows

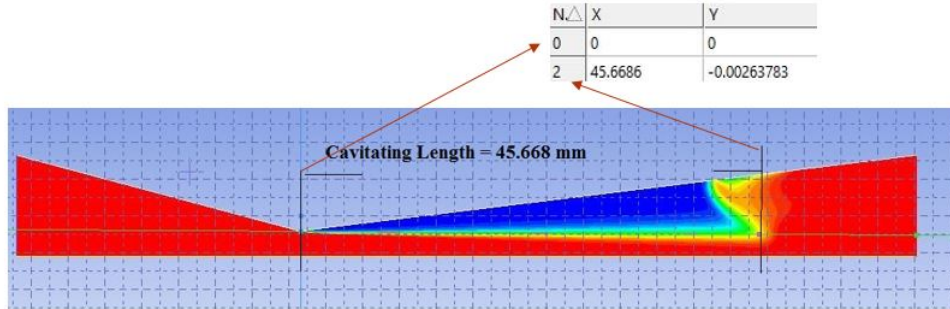


Figure 48: Sample cavitating length measurement for symmetric venturi

From the above calculation, the cavitating length was found by subtracting the x-coordinate at the end of the vapour regime from the x-coordinate at the throat location, which results in the cavitating length of 45.668 mm or 4.56 cm. A similar calculation is done for other cases, and the error in the cavitating length of simulation against the experiments is shown in the following table 49

Test scan data No.	Experimental Cavitating Length (cm)	Simulation Cavitating Length (cm)	Error (%) in cavitation length
396	4.3826	4.560	4.0%
397	4.3826	4.475	2.1%
398	4.3825	4.582	4.5%
399	4.3825	4.582	4.5%

Figure 49: Table showing the error in simulation cavitating length

It is concluded that the above 2D numerical simulation model for cavitating venturi flows resulted in the reasonable benchmark of the experimental test case of Hord et al. [5] and gave an insight for the prediction of cavitating length. The extension of the same for the current symmetric venturi resulted in the prediction of void fraction and the cavitating length, which resulted in an error of less than 4.5%, which is a reasonable comparison of the cavitation length with the actual experimental flow visualization study.

5 Experimental Observations

This section puts forth the experimental observations of two experiments, one with the acrylic venturi test section and the other with the aluminium venturi test section. The acrylic venturi was incompatible with the cryogenic temperature flow conditions, resulting in the crack of the test section itself. Following this, an attempt was made using the same experiment with the aluminium venturi. The flow visualization images during the cavitating time of venturi are presented, and an attempt was made to evaluate the experimental cavitation length from these visualization images.

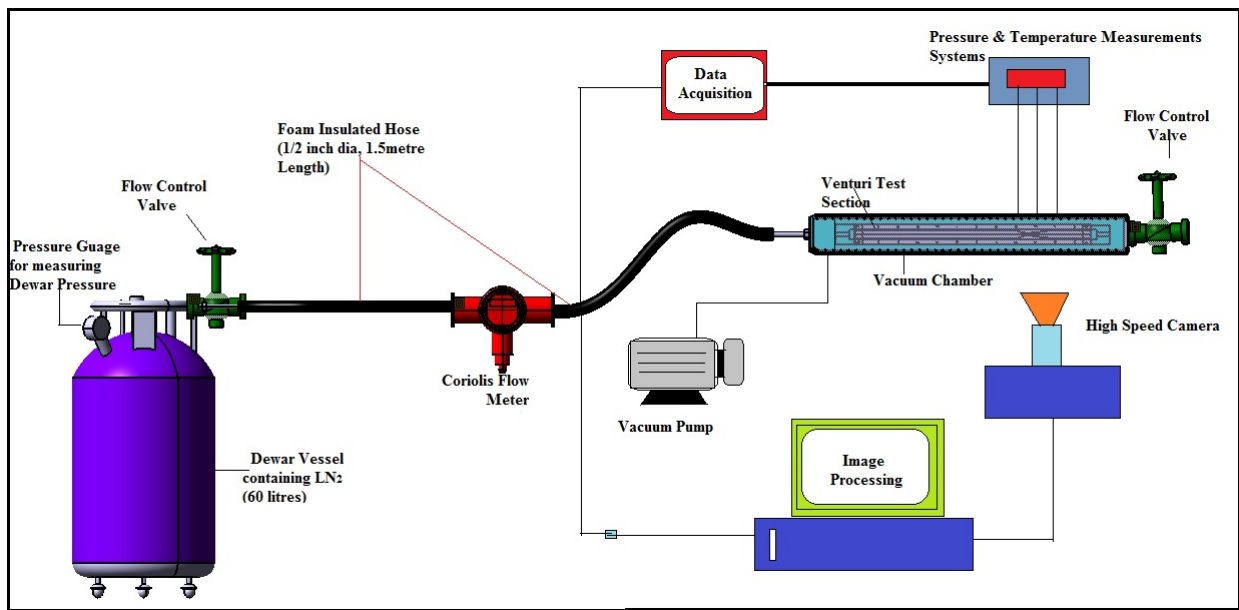


Figure 50: Schematic of the Experimental setup.

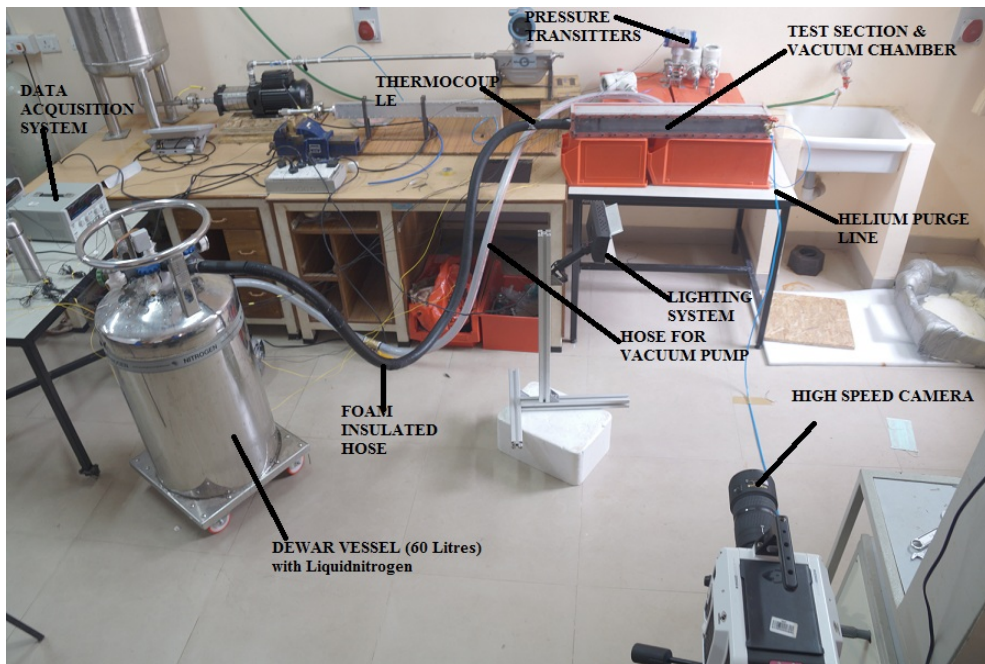


Figure 51: Experimental setup.

5.1 Observations from experiment - 1

The experiment was carried out with an initial Dewar pressure of 2.5 bar, and the outlet of the venturi test section was opened to atmospheric pressure. After an initial transient time for chilling down of the set-up, the developed flow in the test section appeared 4.30 mins from the start of the experiment. Immediately, the nature of the flow of liquid nitrogen turned stratified while flowing inside the test section. This was because of the crack, which developed in the adapter region upstream of the test section, which had a metal-to-acrylic contact. Also, it was observed that the acrylic test section, in due time, resulted in multiple cracks at different spots, which can be seen from the following figure, which was taken from the 42547th frame record of the high-speed camera.

In the above experiment, there was no sign of any developed single-phase flow of liquid nitrogen, and there was no recognized cavitating regime because of the stratified nature of the flow, which was believed to be caused by the cracks in the test section. So, the image data obtained did not give

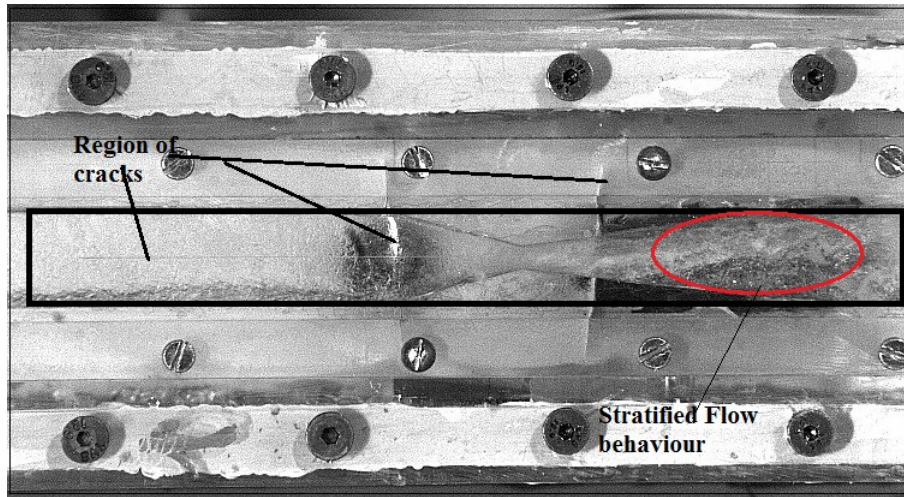


Figure 52: Test section of the experiment - 1

any physical insight into the cavitating nature of the flow and the length. However, the pressure measurement readings closely matched the cavitating regime's operating conditions.

5.2 Observations from experiment - 2

The experiment was carried out with an initial Dewar pressure of 1.2 bar, and the outlet of the aluminium venturi test section was opened to the atmosphere. The time taken for chilling down was reduced compared to the previous experiment, as the entire test section was wound with foam insulation. The developed flow in the test section appeared at 2 min from the start of the experiment. The image was captured at 198th sample scan of the data acquisition system from the video taken by the high-speed camera.

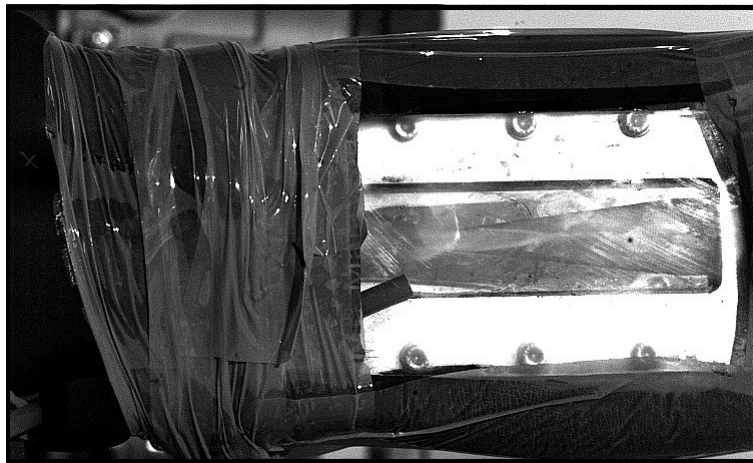


Figure 53: Flow visualization image captured during experiment - 2

The figure 53 shows a distinct vapour regime, which starts from the throat region and extends to some regions in the diverging section of the venturi. The reading from the pressure measurement indicated a near-cavitation operating condition.

The following figure 54 shows the images and corresponding cavitating length for the test cases.





Scan Number	Image	Cavitation Length
396 (197.5 sec)		4.3826 cm
397 (198 sec)		4.3826 cm
398 (198.5 sec)		4.38255 cm
399 (199 sec)		4.38255 cm

Figure 54: Figure showing various test cases

6 Conclusion

The attempted numerical 1D model based on the extension of the Wang and Brennen [9] model with an additional thermal term in line with the numerical 1D model of Rodio [8] was implemented using a finite-difference code in MATLAB. It was inferred that the thermal term in a cavitating water flow had a negligible role to play in bubble growth or collapse. On the other hand, this thermal term had a significant influence on the bubble radius for the liquid nitrogen case. The 2D numerical model was implemented in ANSYS Fluent, and the following are the outcomes of the simulation studies.

- The cavitating length predicted and compared with the experimental results of Hord et al. [5] for validating the developed 2D numerical model.
- A similar procedure was extended for the chosen cavitating venturi using the experimental data as the boundary conditions, and the cavitating length was predicted for the same.

The following are the outcomes from the experimental observations:

- The acrylic venturi test section did not withstand the low-temperature liquid nitrogen flow, resulting in leaks near the upstream venturi and altering the flow pattern to stratified conditions. Hence, a distinct cavitating flow could not be observed in experiment 1.
- The experiment-2, with an aluminum venturi, showed distinct cavitating regimes and the cavitating lengths were estimated from the recorded high-speed camera experimental images.

Acknowledgement We acknowledge Prof.Kannan Iyer and Dr.Nandhakumar (LPSC) for their active discussions. Mr.Dinesh and Mr.Bipin of Thermal Engineering lab are recognized for their assistance with Experiments.

References

- [1] JP Franc, "Physics and control of cavitation," Educational Notes RTO–EN–AVT–143.
- [2] Lord. Rayleigh, 1917, "On the pressure developed in a liquid during the collapse of a spherical cavity", *Philosophical Magazine*, 34(200), pp. 94-98.
- [3] M.S.Plesset et. al., 1949, "The dynamics of cavitation bubbles", *Journal of Applied Mechanics*.
- [4] C.E. Brennen., 1995 "Cavitation and Bubble Dynamics", Oxford University Press., ISBN: 0-19-5094093.
- [5] J. Hord, Anderson L.M, Hall., 1972, "Cavitation in liquid cryogenic : i–venturi", NASA CR-2054.
- [6] Kazuki Niiyama, Satoshi Hasegawa, Shinichi Tsuda, Yoshiki Yoshida, Tsutomu Tamura, Mamoru Oike., 2010, "Thermodynamic effects on cavitation in a cryogenic nozzle flow", I.
- [7] Katsuhide Ohira, Tadashi Nakayama, Takayoshi Nagai, "Cavitation flow instability of subcooled liquid nitrogen in converging-diverging nozzles," *J. Cryogenics* 52(2012)35-44.
- [8] M.G. Rodio, M.G. De Giorgi, A. Ficarella, 2012, "Influence of convective heat transfer modeling on the estimation of thermaleffects in cryogenic cavitating flows", *J. Heat & Mass Transfer* 55 6538–6554.
- [9] Y.C. Wang, C.E. Brennen, "One-dimensional bubbly cavitating flows through a Converging–diverging nozzle," *J. Fluids Eng.* 120 (1998) 166–170.
- [10] A.T.Preston, T.Colonius, C.E.Brennen., 2002, "A Numerical Investigation of Unsteady bubbly cavitating nozzle flows," *Physics of Fluids* 14,300(2002)
- [11] C.F. Delale, G.H. Schnerr, J. Sauer., 2001, "Quasi-one-dimensional steady–state cavitating nozzle flows", *J. Fluid Mech.*, vol. 427., pp. 167–204.
- [12] M.G.Rodio, "Numerical and Experimental Investigation of Water and Cryogenic Cavitating Flows – Phd thesis", *Universit ´a del Salento*(2012).
- [13] D. Albagli, A. Gany., 2003, "High-speed bubbly nozzle flow with heat, mass, and momentum interactions," *Int. J. Heat and Mass Transfer* 46 (2003) 1993–2003.
- [14] W.E. Ranz and W.R. Marshall, "Analysis evaporation from drops – *Chemical Engineering Progress*," 48:141–146, 1952.
- [15] G.H. Schnerr and J. Sauer, "Physical and numerical modeling of unsteady cavitation dynamics," *International Conference on Multiphase Flow, Martin-Luther-Universitt Halle-Wittenberg*, 2001.
- [16] ChanghaiXu, Stephen D. Heister, "Modeling Cavitating Venturi Flows," *JOURNAL OF PROPULSION AND POWER*(2002) Vol.18, No.6.

- [17] Tairan Chen, Guoyu Wang, Biao Huang, Kun Wang, "Numerical study of thermodynamic effects on liquid nitrogen cavitating flows," *Cryogenics*.70(2015) 21-27
- [18] M.S. Plesset and Zwick S.A, "A nonsteady heat diffusion problem with spherical symmetry," *J. Appl. Phys*, 23:95–98, 1952.
- [19] M.G. De Giorgi, A. Ficarella, M.G. Rodio, "Cavitation modeling in cryogenic fluid for liquid rocket engine applications", in: *AIAA-2008-3842*, AIAA, 2008.
- [20] M.G. De Giorgi, P.M. Congedo, M.G. Rodio, A. Ficarella, "Shape optimization for Cryogenic cavitating flows past an isolated hydrofoil", in *FEDSM2008-55119*, ASME, 2008, pp. 7585.
- [21] M.G. De Giorgi, A. Ficarella, "Simulation of cryogenic cavitation by using both inertial and heat transfer control bubble growth", in: *AIAA-2009-4039*, AIAA,2009.
- [22] J.C. Butcher, "Numerical Methods for Ordinary Differential Equation", John Wiley & Sons, 2003.
- [23] "ANSYS FLUENT 12.0, Theory Guide", Ansys, Inc, 2009.
- [24] M. Ishii, S. J. Kataoka, and G. Kocamustafaogullari, "The importance of the interfacial area in two-phase flow analysis," 9th U.S nation. Congr. of Applied Mechanics, pages 73–80, 1982.
- [25] Van Wijngaarden, "On the equations of motion for mixtures of liquid and gas bubbles."
- [26] Van Wijngaarden, "On the collective collapse of a large number of gas bubbles in water", *Proc. Of 11th Int. Cong. Applied Mechanics*, Springer (1964)
- [27] Robert J. Schilling, Sandra L. Harris, "Applied numerical methods for Engineers", Brooks/Cole, 2000, p 374-377.
- [28] R.B.Chapmann, M.S.Plesset., 1972, "Thermal effects in the free oscillation of gas bubbles," *Journal of Basic Engineering* 94, 142-145.
- [29] A. Prosperetti., 1984, "Bubble phenomena in sound fields: part one", *Ultrasonics*, Butterworth & Co. Ltd. 22,69-77.
- [30] Shampine, L.F., "Error Estimation and Control for ODEs", *Journal of Scientific Computing*, 25(2005), 3-16.
- [31] A. Prosperetti., "The thermal behaviour of oscillating gas bubbles", *Journal of Fluid Mechanics* 222 (1991), 587-616.
- [32] Y.C. Wang, "Shock Waves In Bubbly Cavitating Flows - PhD thesis", California Institute of Technology, California, 1996.
- [33] M.G. De Giorgi, D. Bello, and A. Ficarella, "Analysis of thermal effects in a cavitating orifice using rayleigh equation and experiments", *Journal of Engineering for Gas Turbines and Power*, 132:092901(1)–092901(10), 2010..
- [34] M.G. De Giorgi, M.G. Rodio, and A. Ficarella, "Thermodynamic effect on cavitation in water and cryogenic fluids," *ESDA2010-24694*. ASME, 2010
- [35] A. Ulas., 2006, "Passive flow control in Liquid Propellant Rocket Engines with cavitating venturi," *J. Flow measurements and Instrumentation* 17(2006), pp. 93-97.
- [36] Van P.Carey 2008, *Liquid-Vapor phase-change phenomena*, CRC Press.
- [37] Anuja Vijayan, Premchand V, Pradeep Kumar P, Nandakumar K, "On the modelling of cavitating Venturi", *Proceedings of the 6th International and 43rd National Conference on Fluid Mechanics and Fluid Power(FMFP)*, December 15-17, 2016, MNNITA, India

Appendix A: Numerical Method for Modelling 1D Cavitating nozzle / Venturi flow using Matlab

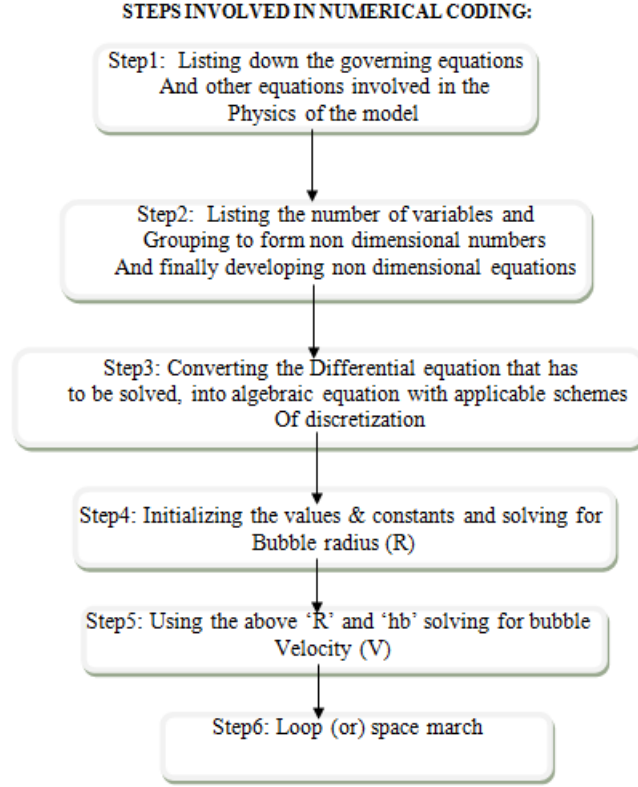


Figure 55: steps involved in numerical coding

Step1: List of Governing Equations and closures:

Continuity and Momentum equation

$$\frac{\partial(1-\alpha)A}{\partial t} + \frac{\partial(1-\alpha)Au}{\partial x} = 0,$$

$$\frac{\partial u}{\partial t} + u \frac{\partial u}{\partial x} = -\frac{1}{2(1-\alpha)} \frac{\partial C_p}{\partial x}$$

Pressure Coefficient

$$C_p(x, t) = \frac{P(x, t) - P_0}{0.5\rho u_0^2}$$

Void fraction equation

$$\alpha(x, t) = \frac{\frac{4}{3}\pi\eta R(x, t)^3}{\left(1 + \frac{4}{3}\pi\eta R(x, t)^3\right)}$$

Modified Rayleigh-Plesset equation

$$\left[R\ddot{R} + \frac{3}{2}\dot{R}^2 \right] + \frac{2S}{\rho_L R} + \frac{4\mu}{\rho_L} \frac{\dot{R}}{R} = \frac{P_{g0}}{\rho_L} \left[\frac{R_0}{R} \right]^{3\gamma} + \frac{[P_\nu(T_\infty) - P_\infty(t)]}{\rho_L} - \frac{dP_\nu}{dT} \frac{\rho_\nu L}{\rho_L} \frac{\dot{R}}{h}$$

Ranz & Marshall convective heat transfer model

$$h_b = \frac{Nu_b K_l}{2R}$$

$$Nu_b = 2 + 0.6Re_b^{\frac{1}{2}} Pr^{\frac{1}{3}}$$

$$Re_b = 2R|\nu - u|/\lambda_l$$

$$Pr = \frac{C_{pl}\mu_l}{K_l}$$

Bubble momentum equation

$$\rho_v \frac{Dv}{Dt} + \frac{1}{2}\rho_l \left(\frac{Dv}{Dt} - \frac{Du}{Dt} \right) = -\frac{\partial P(x,t)}{\partial x} - \frac{3}{8}\rho_l C_D \times \frac{(\nu - u)|\nu - u|}{R}$$

Step2: Non-dimensionalizing the Equations:

All the equations mentioned above were non-dimensionalized by using following dimensionless variables

$$\bar{u} = \frac{u}{u_0}; \bar{x} = \frac{x}{R_0}; \bar{R} = \frac{R}{R_0}; \bar{t} = \frac{tu_0}{R_0}; \bar{v} = \frac{v}{u_0}; \bar{\eta} = \frac{\eta}{R_0^3}; \bar{L} = \frac{L}{R_0}$$

where the subscript "0" corresponds to the upstream value. Some of the non-dimensional numbers, such as

$$Re = \frac{\rho_L u R}{\mu_E}; We = \frac{\rho_L u R}{S}; \sigma = \frac{P - P_v}{\frac{1}{2}\rho_L U^2}$$

After applying these dimensionless terms to the actual steady case equation, the final system of dimensionless equations is of the form

$$(1 - \alpha) \bar{u} \bar{A} = (1 - \alpha_0) = const$$

$$\bar{u} \frac{d\bar{u}}{d\bar{x}} = -\frac{1}{2(1 - \alpha)} \frac{dc_p}{d\bar{x}}$$

$$\bar{R} \left(\bar{u}^2 \frac{d^2 \bar{R}}{d\bar{x}^2} + \bar{u} \frac{d\bar{u}}{d\bar{x}} \frac{d\bar{R}}{d\bar{x}} \right) + \frac{3}{2} \bar{u}^2 \left(\frac{d\bar{R}}{d\bar{x}} \right)^2 + \frac{4\bar{u}}{Re \bar{R}} \frac{d\bar{R}}{d\bar{x}} + \frac{2}{We} \left(\frac{1}{\bar{R}} - \frac{1}{\bar{R}^{3\gamma}} \right) = -\frac{C_p}{2} - \frac{\sigma}{2} \left(1 - \frac{1}{\bar{R}^{3\gamma}} \right) - \frac{dP_v}{d\bar{T}} \frac{L_{ev} \rho_v}{\rho_l h_b} \bar{u} \frac{d\bar{R}}{d\bar{x}}$$

$$\alpha(x, t) = \frac{\frac{4}{3}\pi\bar{\eta}\bar{R}^3}{\left(1 + \frac{4}{3}\pi\bar{\eta}\bar{R}^3 \right)}$$

$$\bar{v} \frac{\partial \bar{v}}{\partial \bar{x}} = \left\{ -\frac{1}{\left(\rho_v + \frac{1}{2}\rho_l \right) \bar{v} u_0^2} \right\} \left\{ \frac{\partial P}{\partial \bar{x}} - \frac{1}{2}\rho_l u_0^2 \bar{u} + \frac{3}{8} \frac{C_D \rho_l}{R} u_0^2 |(\bar{v} - \bar{u})| \right\}$$

The above-governing equations were integrated numerically using a higher-order adaptive Runge-Kutta scheme known as the Dormand-Prince scheme. Details of the adaptive numerical methods are discussed in detail in the next section.

Step3: Numerical solution procedure:

- Dormand-Prince is called adaptive as it attempts to optimize the interval size and reduce the computational cost. The adaptive techniques algorithm should know when the interval (h) size must be adjusted.
- Adaptive methods work by comparing the solution of an Ordinary Differential Equation by two methods, say Euler & Heun's methods[22]. From the solution difference, we find the relative error of the Euler method with respect to Heun's method (as Heun's method is better in comparison with Euler)[22].
- Then, this Error is compared with the allowable error in our computation, and based on that, a scaling factor is found for updating the interval size at each step.

General procedure for finding Scaling parameter for 'h' with an illustrated example

For a given initial value problem,

$$\begin{aligned}y^{(1)}(t) &= f(t, y(t)) \\ y(t_0) &= y_0\end{aligned}$$

Step1: Finding the solution using any two methods of numerical integration. Here, in this case, let the solution be done using Euler and Heun's method

$$\begin{aligned}K_1 &= f(t_k, y_k) \\ K_2 &= f(t_k + h, y_k + hK_1) \\ y_{tmp} &= y_k + hK_1 \\ z_{tmp} &= y_k + h \frac{K_1 + K_2}{2}\end{aligned}$$

Where y_{tmp} and z_{tmp} are the solutions obtained from Euler and Heun's methods, respectively.

Step2: The difference between the two solutions, $|y_{tmp} - z_{tmp}|$ is the Error. This error obtained is the error in the Euler method compared to Heun's method, and the error is of order $O(h^2)$. Therefore, error can be written as a function of h^2

$$|y_{tmp} - z_{tmp}| = Ch^2 \tag{20}$$

Step3: Substituting scaling factor. Scaling 'h' by some factor 's'

$$|y_{tmp} - z_{tmp}| = Ch^2 = C(sh^2) \tag{21}$$

Step4: Comparing the Error with allowable error & finding 's'

$$C(sh^2) < \varepsilon_{abs}$$

The contribution of the maximum error at the k^{th} step should be proportional to the width of the interval relative to the whole interval

$$\begin{aligned}C(sh)^2 &< \varepsilon_{abs} \frac{sh}{t_f - t_0} \\ C(sh)^2 &= \frac{1}{2} \varepsilon_{abs} \frac{sh}{t_f - t_0} = \frac{\varepsilon_{abs} sh}{2(t_f - t_0)}\end{aligned} \tag{22}$$

$$\Rightarrow s(Csh^2) = \frac{\varepsilon_{abs} h}{2(t_f - t_0)} \tag{23}$$

Putting equation 20 in 22

$$\begin{aligned}s|y_{tmp} - z_{tmp}| &= \frac{\varepsilon_{abs} h}{2(t_f - t_0)} \\ \Rightarrow s &= \frac{\varepsilon_{abs} h}{2(t_f - t_0) |y_{tmp} - z_{tmp}|}\end{aligned} \tag{24}$$

Updating 'h',

$$h^* = s \times h$$

where, h^* is the updated value of h.

Depending on the value of 's', the value of 'h' is updated as follows

- If $s \geq 2$, $h^* = 2 \times h$
- If $1 \leq s < 2$, $h^* = h$
- If $s < 1$, $h^* = \frac{h}{2}$ (and try again)

Algorithm for Dormand Prince Adaptive method

In the Dormand Prince adaptive method, RK4 and RK5 methods are compared generally

Step1: Finding the slopes k_1 to k_7 .

$$k_1 = hf(t_k, y_k)$$

$$k_2 = hf\left(t_k + \frac{1}{5}h, y_k + \frac{1}{5}k_1\right)$$

$$k_3 = hf\left(t_k + \frac{3}{10}h, y_k + \frac{3}{40}k_1 + \frac{9}{40}k_2\right)$$

$$k_4 = hf\left(t_k + \frac{4}{5}h, y_k + \frac{44}{45}k_1 - \frac{56}{15}k_2 + \frac{32}{9}k_3\right)$$

$$k_5 = hf\left(t_k + \frac{8}{9}h, y_k + \frac{19372}{6561}k_1 - \frac{25360}{2187}k_2 + \frac{64448}{6561}k_3 - \frac{212}{729}k_4\right)$$

$$k_6 = hf\left(t_k + h, y_k + \frac{9017}{3168}k_1 - \frac{355}{33}k_2 - \frac{46732}{5247}k_3 + \frac{49}{176}k_4 - \frac{5103}{18656}k_5\right)$$

$$k_7 = hf\left(t_k + h, y_k + \frac{35}{384}k_1 + \frac{500}{1113}k_3 + \frac{125}{192}k_4 - \frac{2187}{6784}k_5 + \frac{11}{84}k_6\right)$$

Step2: Finding the solution using RK4 and RK5 method.

The solution by Runge-Kutta 4th order method is given by:

$$y_{k+1} = y_k + \frac{35}{384}k_1 + \frac{500}{1113}k_3 + \frac{125}{192}k_4 - \frac{2187}{6784}k_5 + \frac{11}{84}k_6$$

The solution by Runge-Kutta 5th order method is given by:

$$y_{k+1} = y_k + \frac{5179}{57600}k_1 + \frac{7571}{16695}k_3 + \frac{393}{640}k_4 - \frac{92097}{339200}k_5 + \frac{187}{2100}k_6 + \frac{1}{40}k_7$$

Step3: The Error in the RK4 method is calculated by finding the difference between the two solutions. The error for the Dormand Prince method is as shown below:

$$|z_{k+1} - y_{k+1}| = \left| \frac{71}{57600}k_1 - \frac{71}{16695}k_3 + \frac{71}{1920}k_4 - \frac{17253}{339200}k_5 + \frac{22}{525}k_6 - \frac{1}{40}k_7 \right|$$

Step4: Finding the scaling factor and optimum interval size. The scaling factor for Dormand Prince is given by

$$s = \left(\frac{\varepsilon h}{2|z_{k+1} - y_{k+1}|} \right)^{\frac{1}{5}}$$

The optimum interval size is given by Error prediction methods by Shampine[22]

$$h_{opt} = sh$$

The above algorithm is incorporated in Matlab coding, and the model was solved for cases involving water and liquid nitrogen.